Numerical Modelling and Performance Analysis of a Packed Bed Electric Thermal Energy Storage System Integrated with a Rankine Cycle

Master Thesis

Jakob Nørregård Olesen 10^{th} semester AAU Energy

Aalborg University
Department of Energy

Department of Energy
Aalborg University
http://www.aau.dk

AALBORG UNIVERSITY
STUDENT REPORT

Title:
Numerical Modelling and Performance Analysis of a Packed Bed Electric Thermal Energy Storage System Integrated with a Rankine Cycle

Theme:
Master Thesis

Project Period:
Fall Semester 2025

Participant(s):
Jakob Nørregård Olesen

Supervisor(s):
Kim Sørensen
Thomas Condra

Number of Pages: 69

Date of Completion:
May 28th - 2025

Abstract:

The transition towards renewable energy sources necessitates efficient energy storage solutions to balance supply and demand fluctuations. This thesis presents a numerical modeling and performance analysis of a packed bed thermal energy storage (PBTES) system integrated with a Rankine cycle. The study develops a one-dimensional, transient numerical model to simulate temperature evolution and heat transfer during charging and discharging cycles. The model is validated against existing reference data from a PBTES facility, demonstrating its reliability in predicting system behavior. A parametric sensitivity analysis is conducted exploring the effects of particle size, mass flow rate, and void fraction on temperature distribution and pressure loss. To evaluate system performance during discharge, both single-pressure and *Dual- Pressure* (DP) Rankine cycles are integrated with a Heat Recovery Steam Generator, and metrics such as thermal efficiency, power output, and round-trip efficiency are assessed. The integration of a DP Rankine cycle improves heat recovery while maintaining a thermal efficiency of approximately 36%. In conclusion, this thesis demonstrates the viability of a packed bed thermal energy storage system integrated with a Rankine cycle for flexible, grid-scale energy storage.

Executive Summary

As energy systems shift toward renewables, the need for effective storage technologies to manage supply and demand fluctuations becomes increasingly important. This thesis presents an in-depth numerical modeling and performance analysis of a packed bed thermal energy storage (PBTES) system integrated with a Rankine cycle. By addressing the challenges of intermittent renewable energy sources, this research explores the feasibility and performance of PBTES through numerical modeling, sensitivity analysis, and system integration assessments.

The system concept involves a packed bed filled with rock material through which air is circulated during charging and discharging cycles. In the charging phase, electric energy heats air, which transfers thermal energy to the solid particles in the bed. In the discharging phase, cold air is drawn through the packed bed, recovering stored heat and transferring it to a *Heat Recovery Steam Generator* (HRSG), which drives a Rankine cycle to generate electricity.

The study introduces a one-dimensional, transient numerical model capable of simulating the temperature evolution and heat transfer in a cylindrical packed bed during both charging and discharging operations. The model employs explicit finite-difference schemes to solve the energy conservation equations for both the solid (rock) and fluid (air) phases and includes considerations for thermal losses and pressure loss. Verification of the model was performed against data from a commercial-scale ETES demonstration plant developed by Siemens Gamesa in Hamburg, Germany. The numerical results exhibited close agreement, with temperature profiles and thermal behavior closely matching the benchmark data. This established the model's reliability for simulating transient thermodynamic phenomena in PBTES systems.

A sensitivity analysis was conducted for the packed bed system to investigate the impact of different parameters including mass flow rate, particle diameter, and void fraction. Increasing mass flow rate was found to improve heat transfer rates, although at the cost of elevated pressure losses due to increased friction. A moderate void fraction around a value of 0.45 yielded a balance between heat transfer efficiency and manageable pressure loss across the packed bed. Similarly, while smaller particle diameters enhanced heat exchange due to increased surface contact, they also resulted in higher airflow resistance, necessitating careful consideration of system design trade-offs.

The integration of a *Dual-Pressure* (DP) Rankine cycle was explored to assess its potential of heat recovery and improvement in the thermal efficiency. A comparative analysis between single-pressure and DP configurations revealed that operating with two pressure levels 67 bar for high pressure and 20 bar for low pressure increased the utilization of recovered thermal energy while maintaining a thermal efficiency of approximately 36%. Lower LP evaporator pressures improved heat extraction, reducing air outlet temperatures and enhancing steam generation, though this also resulted in a minor reduction in the thermal efficiency. Additionally, sensitivity analysis of air inlet temperature into the HRSG demonstrated that higher temperatures led to greater electricity generation, with an inlet

air temperature of 650°C yielding a net work output around 2 MW. From an economic perspective, the Levelized Cost of Electricity was analyzed to determine the feasibility of implementing the PBTES system at scale.

Although the DP Rankine cycle and the inclusion of a deaerator improved efficiency, *Capital Expenditures* (CAPEX) needed to remain below a breakeven threshold to ensure viability. The analysis indicated that additional CAPEX should not exceed 239 €/kWh beyond a baseline of 100 €/kWh, reinforcing the necessity of balancing technical improvements with financial constraints. In conclusion, this thesis demonstrates that a one-dimensional, transient numerical model effectively simulates the thermal behavior of a PBTES system and provides valuable insights into its interaction with a Rankine cycle. The research highlights the importance of balancing the packed bed design parameters, such as mass flow rate, particle diameter, and void fraction, to achieve the best trade-offs between efficiency, thermal performance, and operational costs. Furthermore, integrating a DP Rankine cycle offers enhanced heat recovery potential, improving the overall feasibility of the Packed Bed Thermal Energy Storage System for renewable energy integration. Future research should focus on refining numerical modeling techniques, exploring alternative storage media, and conducting real-world economic assessments to further validate the system's commercial viability.

Preface

The following master thesis has been done in 10^{th} semester of the master´s degree at Aalborg University. I would like to show my most appreciation and thanks to my supervisors at Aalborg University Kim Sørensen and Thomas Condra for their guidance throughout the project.

Reading Guide

The citations have been done using the Harvard method where the citations will be shown as [Author(s), year]. The citations follow their references in the bibliography. Chapters, sections, figures, tables and equations are labelled in the text. The numbering of these labels is in chronological order and chapter-wise. Throughout the report, the symbols, abbreviations and subscripts is located in the Nomenclature. The following software has been used in this project:

- CoolProp
- Engineering Equation Solver (EES)
- Microsoft Office
- Overleaf LaTeX®
- MATLAB
- Python

Jakob Olesen
jnol20@student.aau.dk

Signature: Jakob Olesen

Nomenclature

Standard SI-Units will be used

Symbol	Description	SI Unit
A_c	Cross-sectional Area	[m^2]
A_s	Surface Area	[m^2]
Bi	Biot number	[-]
c_p	Specific heat capacity	[J/(kg·K)]
d_p	Particle diameter	[m]
D	Diameter	[m]
Δz	Spatial step size	[m]
Δt	Time step size	[s]
η_{charge}	Efficiency during charge cycle	[%]
$\eta_{discharge}$	Efficiency during discharge cycle	[%]
η_{fan}	Fan efficiency	[%]
η_{h2p}	Heat-to-power efficiency	[%]
η_{p2h}	Power-to-heat efficiency	[%]
η_{p2p}	Round-trip (power-to-power) efficiency	[%]
E	Energy	[J]
G	Mass Flux	[kg/(m^2·s)]
h	Convective heat transfer coefficient	[W/(m^2·K)]
h	Enthalpy	[J/kg]
k	Thermal conductivity	[W/(m·K)]
L	Length	[m]

Symbol	Description	SI Unit
L_c	Characteristic Length	[m]
m	Mass	[kg]
$\dot{m}$	Mass flow	[kg/s]
n	Number of years	[years]
N	Number of Nodes	[-]
Nu	Nusselt Number	[-]
P	Pressure	[Pa]
ΔP	Pressure loss	[Pa]
Pr	Prandtl Number	[-]
Q	Thermal Energy	[J]
$\dot{Q}$	Heat Transfer Rate	[W]
Re	Reynolds Number	[-]
r	Discount Rate	[-]
r	Radius	[m]
R	Thermal Resistance	[K/W]
s	Specific entropy	[J/(kg·K)]
t	Time	[s]
T	Temperature	[K or °C]
U	Overall Heat Transfer Coefficient	[W/(m^2·K)]
UA	Thermal Transmittance	[W/K]
V	Volume	[m^3]
V	Average Velocity	[m/s]
$\dot{W}$	Power	[W]
x	Thickness	[m]

Standard SI-Units will be used

Symbol	Description	SI Unit
α	Thermal diffusivity	m^2/s
Δ	General symbol for change/difference (e.g. ΔT)	Depends on context
ϵ	Void fraction of the packed bed	[-]
η	General efficiency (e.g. charge, discharge, Rankine cycle)	[-]
μ	Dynamic viscosity	kg/(m·s)
ν	Kinematic viscosity	m^2/s
ρ	Density	kg/m^3

Abbreviations

Abbreviation	Description
CAPEX	Capital Expenses
CHP	Combined Heat and Power
DP	Dual-Pressure
ES	Energy Storage
EES	Electric Energy Storage
ETES	Electric Thermal Energy Storage
HRSG	Heat Recovery Steam Generator
LCOE	Levelised Cost of Electricity
LMTD	Logarithmic Mean Temperature Difference
LP	Low Pressure
OPEX	Operational Expenses
PCM	Phase Change Material
HP	High Pressure
PBTES	Packed Bed Thermal Energy Storage
PHS	Pumped Hydroelectric Storage
PV	Photovoltaic
SP	Single-Pressure
TES	Thermal Energy Storage
T-s	Temperature-Entropy (diagram)
WEC	Wind Energy Converter

Contents

List of Figures

List of Tables

Chapter 1

Introduction

Climate change is one of the major global challenges of the 21st century. The atmospheric CO_2 concentration is increasing, particularly due to the combustion of fossil fuels for energy production, leading to rising global temperatures. This temperature increase leads to serious consequences in many regions around the world. To mitigate climate change, it is vital to reduce CO_2 emissions [IPPC, 2021]. One key strategy is the transition to renewable energy sources and electrification, particularly by replacing fossil fuels with solar and wind power [Paraschiv and Paraschiv, 2023]. *Wind Energy Converters* (WECs) and *Photovoltaic* (PV) are among the most widely used renewable technologies for generating electricity from renewable sources. However, a drawback of WECs and PV is the intermittent nature of wind and solar energy. Their availability fluctuates seasonally, daily, and with weather conditions, and often does not not align with electricity demand patterns [Eggers et al., 2022].

To address this challenge and enable a higher share of variable renewable energy, improved integration between the electricity, heating, and mobility sectors is required. *Energy storage* (ES) plays a essiential role in this integration. ES can be used to balance supply and demand by storing excess energy when the energy production exceeds consumption and releasing it when needed. In recent years, ES has gained increased attention due to the evolving nature of the energy market [Eller and Gauntlett, 2017]. The variability of solar and wind generation, combined with time-dependent electricity demand, creates challenges for both the power grid and energy markets. These challenges include maintaining grid stability and responding to market fluctuations. Moreover, imbalances between production and consumption frequently cause large and sudden changes in energy prices [Elsevier, nd]. These dynamics are illustrated in Figure 1.1.

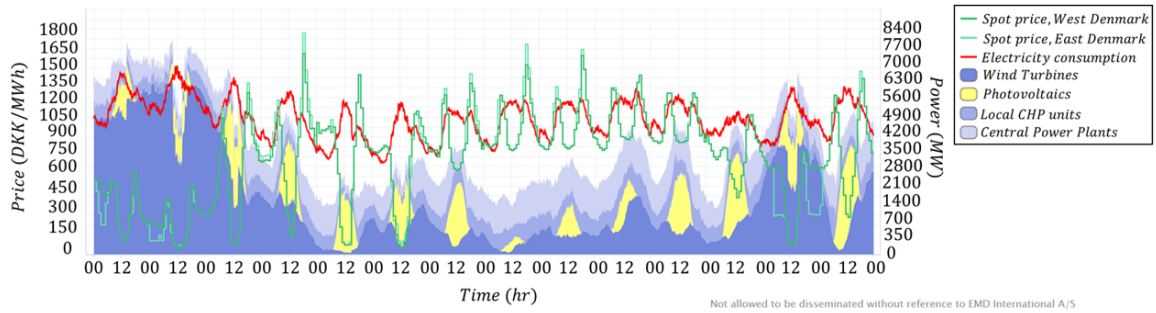

Figure 1.1: Hourly variation in renewable energy production and electricity prices over a 14-day period in Denmark (2025). The graph shows electricity spot prices (DKK/MWh) and power generation/consumption (MW) for both West and East Denmark. It includes data on electricity consumption and the contributions from wind power, solar PVs, local (CHP) units, and central power plants.[International, 2025].

Figure 1.1 shows Denmark's electricity spot prices and electricity power production from various sources including wind turbines, PV, local *Combined Heat and Power* (CHP) units and CHP plants over the period from March 4 to March 17, 2025. The green lines represent spot prices in West and East Denmark, while the red line indicates electricity consumption. The stacked blue and yellow areas show the contributions from different power sources. It is evident that fluctuations in renewable energy generation correspond closely with changes in electricity prices and the output from central power plants. This variability highlights the need for effective ES solutions to enhance grid flexibility, improve the utilization of renewable energy, and stabilize electricity prices. By storing surplus energy during periods of low demand and low electricity prices, and releasing it during times of high demand and high prices, ES systems can help balance supply and demand. In doing so, ES not only supports grid stability but also reduces reliance on fossil-based backup generation and mitigates large price fluctuations in the electricity market. ES technologies are generally categorized into short-term and long-term applications [Mostafa et al., 2020], the most common ES technologies include *Pumped Hydroelectric Storage* (PHS), Thermal Energy Storage (TES), and *Electric Energy Storage* (EES).

PHS is a ES technology that stores potential energy by moving water between two reservoirs located at different elevations. When electricity is needed, water is realeased from the upper reservoir to the lower reservoir, driving a turbine to generate electricity [Elsevier, nd]. Another common ES technology involves the use of batteries. Particularly, lithium batteries are currently in operation all over the world and are considered a mature EES method. These batteries operate through chemical reactions and are known for their rapid response times, making them well-suited for grid stabilization and short-term storage. However, their primary limitation is a relatively short lifespan, due to a limited number of charge-discharge cycles [Elsevier, nd]. TES is another promising aproach capable of storing heat for both short and long durations. TES systems are increasingly being applied in power generation, industrial processes, and heating and cooling applications. They typically involve storage tanks filled with materials such as water or rocks. TES is especially valuable in high-temperature applications, such as waste heat recovery, power-to-heat solutions in industry, and enhancing the operational flexibility of thermal power plants [von der Heyde, 2022].

These ES technologies presented vary in their maturity, cost, and performance. While some are commercialized, others are still undergoing development and testing. A comparison of these technologies based on key performance metrics, economic factors, and energy characteristics is presented in Table 1.1.

Parameters	Li-ion battery	PHS	TES
Round-trip efficiency, [%]	90	85	35-50
Price per kWh_e, $[/kWh_e]$	300-350	106-200	100-300
Lifetime, [Years]	5-10	30-50	15-20
Energy Density, [Wh/kg]	100-265	0,5-3	80-250

Table 1.1: Comparison of ES technologies (Li-ion battery, PHS, TES) based on efficiency, cost, lifespan, and energy density [Elsevier, nd] [von der Heyde, 2022].

.
Table 1.1 presents a comparative overview of the Li-ion batteries, PHS and TES based on key performance and economic indicators. Both PHS and Li-ion batteries exhibit relatively high round-trip efficiencies around 85% and 90%, respectively making them well-suited for applications requiring frequent charge-discharge cycles and quick energy access. However, these technologies also come with drawbacks. Li-ion batteries, for example, have a short operational lifetime and high cost per unit of stored electricity. PHS, while more cost-effective over its lifetime, is geographically constrained and has low energy density, making it impractical in many locations. TES, on the other hand, although less efficient in terms of round-trip efficiency, offers several advantages. It provides moderate to high energy density, competitive costs of electricity per kWh, and longer lifetimes than Li-ion batteries. Furthermore, TES is highly scalable and particularly suitable for integrating with heating systems, industrial waste heat recovery, and power-to-heat applications. This thesis, therefore, focuses on the TES. The three most utilised TES are sensible heat storage, latent heat storage, and thermochemical heat storage, which will be considered next.

1.1 Thermal Energy Storage

1.1.1 Latent Heat Storage

Latent heat storage involves storing or releasing thermal energy during its phase change at a constant temperature. This method utilizes *Phase Change Materials* (PCMs), which absorb or release latent heat as they transition between solid and liquid phases. Common PCMs include paraffins, salt hydrates, and metallic alloys. A key advantage of latent heat storage is its high ES density. However, challenges include the relatively high cost of both storage systems and PCMs, as well as limitations in thermal conductivity and long-term stability, which can affect performance over repeated cycles [Koefoed, 2013].

1.1.2 Thermochemical Storage

Thermochemical ES relies on reversible chemical reactions to store and release thermal energy. In this process, a thermochemical material undergoes either a reversible physical transformation involving two or more substances, or a reversible chemical reaction. During the endothermic (charging) phase, heat is absorbed to drive the forward reaction and store energy. In the exothermic (discharging) phase, the reverse reaction releases the stored heat for use in various energy applications. Some examples that can be used for thermochemical ES involve steam methane reforming or the ammonia dissociation process [Koefoed, 2013].

1.1.3 Sensible Heat Storage

Sensible heat storage is based on raising or lowering the temperature of a storage medium typically involving a solid or liquid without any phase change. It is a mature and well-established technology, frequently applied in industrial processes, solar thermal plants, and waste heat recovery systems. The performance of this storage method depends primarily on the specific heat capacity, thermal conductivity, and operating temperature range of the storage medium. Common materials include water, molten salts, and rocks, often

utilized in thermally insulated tanks to minimize heat loss. For high-temperature applications, solid materials are frequently preferred due to their lower cost and higher operating temperatures compared to liquids. A particularly cost-effective and scalable approach involves packed beds filled with rocks, which is the focus of this thesis [Khan et al., 2022]. This will be expanded upon further in the following section.

1.2 Packed Bed Thermal Energy Storage

Packed beds of rocks represent a promising solution for high-temperature TES due to their low material cost, high availability, and wide operational temperature range, with applicability up to 800 °C [Marongiu et al., 2019]. Additional advantages include minimal material degradation over time, low safety risks, and a rapid thermal response. These features make packed beds particularly attractive for industrial-scale applications, especially where cost-effective and durable storage is essential. The main drawback of this technology is its lower round-trip efficiency compared to other ES technologies, and large fans are required, which will result in relatively high operational costs. A packed bed TES consists of solid particles, such as rocks that vary in size and shape. A *Heat Transfer Fluid* (HTF) flows through these particles to store and transfer thermal energy. The most commonly utilized HTF in a packed bed TES involves the fluids, air, water and molten salts [Zanganeh et al., 2012].

The HTF flows through the voids between solid particles in the bed, allowing direct thermal interaction with the storage material. During the charging phase, hot HTF enters the bed in one direction, transferring heat to the solid particles and raising their temperature. In the discharging phase, the flow direction is reversed: colder HTF enters, absorbs heat from the hot solid particles and leaves the packed bed at an elevated temperature. This is illustrated in Figure 1.2

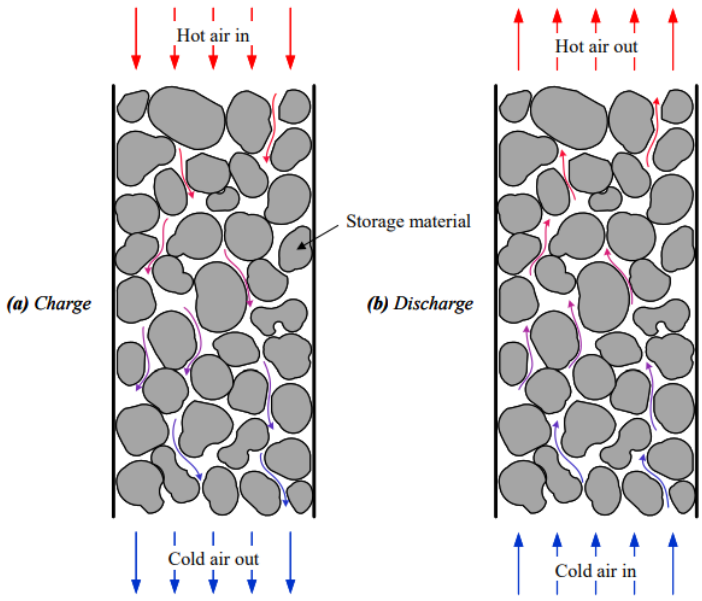

Figure 1.2: Packed bed TES with air blowing through storage material in (a) charging mode and (b) discharging mode [Wahab et al., 2023].

In practical applications, hot air is used to heat the cold stones during charging. During discharge, cold air is passed in the reverse direction to extract the stored heat. This configuration is particularly suitable for waste heat recovery systems and power generation applications, where high-temperature heat can be cyclically stored and released with minimal degradation of materials [Muhammad, 2022]. Furthermore, the utilization of the packed bed are well-aligned with dynamic electricity pricing strategies. For instance, they can be charged during periods of low electricity prices by operating fans to heat the bed using surplus energy at low electricity prices. The stored heat can then be discharged when needed during higer electricity prices, improving the system's economic viability and integration with intermittent renewable energy sources [Zanganeh et al., 2012].

One type of utilization involves a so-called *Electric Thermal Energy Storage* (ETES) system, which uses a packed bed as a high-temperature TES combined with a Rankine cycle for power generation [von der Heyde, 2022]. A system composition of this is shown in Figure 1.3

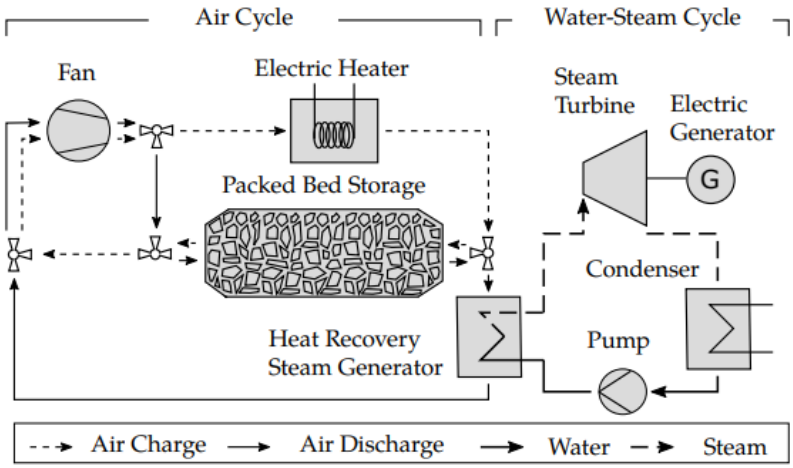

Figure 1.3: Schematic of the ETES involving a combined air and water-steam cycle for energy storage and recovery, showing key components such as packed bed storage, a steam turbine, and heat recovery systems. [von der Heyde, 2022].

This system is charged using electricity from wind and solar or the grid, which can be used to heat the air using an electric heater to be stored in the packed bed TES. A fan moves the air in the closed cycle through the electric heater and the packed bed in the charging process. This thermal energy is stored until electricity demand increases or market prices justify power generation. In the discharging phase, the flow direction of the air is reversed. The ambient or cooler air passes through the hot packed bed, absorbing the stored thermal energy. The heated air then enters a *Heat Recovery Steam Generator* (HRSG), where it transfers its energy to a working fluid, typically water, in the Rankine cycle.
The HRSG functions similarly to that in conventional thermal power plants, however instead of using flue gas from fuel combustion, it is powered by hot air. It typically includes economizer, evaporator, and superheater sections, enabling efficient transfer of thermal energy across different temperature levels of the steam generation process. Once the steam reaches the desired temperature and pressure, it expands through a steam turbine, producing mechanical work that is converted into electricity via a generator. This electricity can then be supplied back to the grid.

After expansion, the steam is condensed in a condenser, which may be cooled using either cooling towers or repurposed for domestic heating applications such as district heating networks, enhancing the overall system efficiency. The condensed water is then pressurized by a feedwater pump and returned to the HRSG, closing the Rankine cycle loop [von der Heyde, 2022].

1.2.1 Applications of Packed Bed Thermal Energy Storage

The ETES system can be used in various applications including flexible power-to-heat, cogeneration of heat and power or conversion of existing power plants into ES units [Rabi' et al., 2024]. During the discharge phase, coupling the ETES with a CHP configuration increases the utilization rate of stored thermal energy by enabling the simultaneous generation of electricity and useful heat. In this mode, heat can be extracted via steam and supplied directly to industrial processes or district heating networks [von der Heyde, 2022]. ETES systems enable an electricity-led operation, providing flexibility to both the electricity and heat sectors, particularly during periods of fluctuating renewable energy generation. In power-to-heat applications, where only thermal energy is required, the absence of a water-steam cycle significantly reduces the associated cost compared to power-to-power systems. In some cases, the HTF in this case air can be used directly, eliminating the need for a HRSG altogether [von der Heyde, 2022]. The ETES can be classified as thermo-mechanical ES technology and more specifically as Carnot Battery, which converts electric energy to thermal energy for charge and uses a heat engine, typically a Rankine cycle to regenerate electricity from the stored thermal energy during discharge [Dumont et al., 2020].

Integrating ETES into existing CHP plants is beneficial, as it allows the shared use of the water-steam cycle and grid infrastructure. For example, during CHP operation, fossil fuels are commonly utilized to meet electricity demand spikes. In such cases, ETES can supply industrial heat, allowing the main power plant to curtail operations or avoid firing fossil fuel-based backup heat sources [von der Heyde, 2022]. A major strength of the ETES concept is its use of commercially available components for the charge and discharge processes, especially on the targeted multi-MW scale. One of the ETES demonstration plants was commissioned in 2019 in Hamburg, Germany, by Siemens Gamesa Renewable Energy. The demonstration plant incorporates a high-temperature packed-bed TES where crushed volcanic rock is used as the storage medium. The rocks are contained within a concrete structure, and the airflow direction is horizontal through the packed bed. Insulation involving aerated concrete and rock wool is used to reduce thermal losses. The packed bed is supported by grating structures at the hot and cold ends. A grating is used to hold up the packed bed at the hot and cold sides. The storage and the entire air system are working near atmospheric pressure to allow for a simple plant setup and use of standard materials [von der Heyde, 2022]. Some of the key characteristics of the plant are shown in Table 1.2

ETES	Value
Rated Power Electric Heater	5.4 $MW_{electric}$
Rated Power Turbine	1.4 $MW_{electric}$
HRSG Power	5 $MW_{thermal}$
Rankine Efficiency	28 %
Power-to-Power Efficiency	25 %
Thermal Storage Capacity	130 MWh
Steam Temperature	480 °C
Steam Pressure	67 bar
Storage Material Weight	1×10^6 kg
Air Charge Temperature	650 °C
Air Discharge Temperature	500 °C
Volume of Packed Bed	700 m^3

Table 1.2: Key system parameters of the ETES, including rated power, efficiency, thermal storage capacity, temperatures, pressures, and physical dimensions, essential for understanding performance and design [von der Heyde, 2022].

Table 1.2 presents the main technical specifications of the ETES demonstration plant developed by Siemens Gamesa Renewable Energy in Hamburg. The electric heater has a rated power of 5.4 MW, representing the charging capacity of the system when converting electricity into high-temperature heat. During discharge, the system is capable of generating 1.4 MW of electrical power through the turbine and supplying 5 MW of thermal power via the HRSG. The heat-to-power efficiency of the Rankine cycle is reported to be 28%, whereas the power-to-power efficiency is 25% for the ETES plant. Although the ETES by [von der Heyde, 2022] have been shown to be commercially mature, the packed bed design involves several challenges. These include uneven airflow distribution, non-uniform heat transfer and temperature gradients within the bed, and significant pressure losses as air flows through the packed bed [Allen et al., 2013]. These pressure losses increase the energy demand of the fan, thereby reducing the overall system efficiency. Key thermal and geometric parameters including mass flow rate, void fraction, pressure loss, and particle size must be carefully analyzed and optimized to minimize energy losses and improve overall storage utilization [Anderson et al., 2015, Mao, 2016]. It is thereby essential to investigate some of these parameters to reduce energy consumption and increase the utilization of the packed bed for electricity generation.

1.3 Summary

As outlined in the introduction, there is a growing need for ES solutions that ensure a stable supply of clean energy, independent of fluctuating renewable sources. TES offers a cost-effective alternative to other storage methods, with packed bed TES emerging as a promising option due to its low material costs and suitability for high-temperature operation. Packed bed TES can be effectively integrated into ETES that incorporates a Rankine cycle for combined power and heat generation, providing a flexible energy solution. However, challenges such as thermal stratification, pressure loss, and flow distribution must be examined to enhance the ETES performance, leading to the formulation of the following problem statement.

Chapter 2

Problem Statement

A *Packed Bed Thermal Energy Storage* (PBTES) system offers a promising solution to address the mismatch between variable renewable energy production and energy demand. By storing thermal energy during periods of low electricity prices and release it when electricity are needed or when the prices are high, PBTES systems can enhance grid flexibility and support a more stable and sustainable energy supply. This thesis focuses on the numerical modelling of the PBTES and analyzing key parameters that influence the behaviour and performance of both the packed bed and the integrated Rankine cycle. Furthermore, the feasibility and overall performance of the PBTES and combined Rankine cycle are examined in order to assess the viability of the combined system. The following research questions are considered in relation to this.

- How can a one-dimensional, transient numerical model be used to simulate temperature evolution and heat transfer in a packed bed TES system during charging and discharging?

- How does variation in particle size, mass flow rate, and void fraction influence temperature evolution, heat transfer and pressure loss in the packed bed TES system?
- How does the integration of a dual-pressure Rankine cycle during discharge impact the thermal efficiency of the combined packed bed TES system, and how do changes in pressure and temperature influence this effect?

2.1 Methodology

To address the research questions, a comprehensive model of the combined PBTES and the associated Rankine cycle is developed using Python and MATLAB. This model enables detailed calculations and performance simulations of the system's main components, including the PBTES, HRSG, electric heater, fan, pump, turbine, and condenser. The PBTES is represented through a one-dimensional, transient numerical model that captures the temperature distribution within the storage medium over time and space during both charging and discharging phases. The rest of the components involved in the combined system are modelled based on energy and mass balances. To validate the reliability of the PBTES model, simulation results are compared with operational data from a similar system described by [von der Heyde, 2022]. In addition, a sensitivity analysis is carried out on key parameters, such as mass flow rate and void fraction, to evaluate their impact on system performance. This analysis helps identify critical trade-offs and design considerations that can enhance the efficiency and operational flexibility of the integrated system.

2.2 Limitations

Several limitations and assumptions is made in the modelling of the PBTES and the integrated Rankine cycle, which should be kept in mind when interpreting the results. First, the HRSG is modelled as an adiabatic heat exchanger, meaning that heat losses to the surroundings are not accounted for. Pressure losses in the condenser and HRSG are neglected. Furthermore, auxiliary components such as pipes and valves are not included in the model of the PBTES. The transient behaviour of the system is only considered within the PBTES unit, while all other components are assumed to operate under steady-state conditions. Additionally, the dynamic behaviour within the packed bed is not taken into account. The thermal storage process is limited to sensible heat transfer within the solid rock material, where latent heat effects and thermal degradation of the material are not considered. No experimental work has been conducted in this thesis. Instead, the numerical model has been validated using data available in the literature. Finally, extended economic analysis and feasibility study of the integrated system is beyond the scope of this thesis and has not been carried out.

Chapter 3

Modelling

The following chapter presents the modeling approach for each component of the system including the packed bed TES integrated Rankine cycle, and auxiliary components involving an electric heater and fan. It also compares *Singe-Pressure* (SP) and *Dual-Pressure* (DP) Rankine cycle configurations. Finally, system efficiencies are incorpated to assess overall performance.

3.1 Modelling of the Packed Bed Thermal Energy Storage

The system operates by storing thermal energy using electricity during charging and converting it back into electricity during discharging for consumption. In the charging phase, a fan circulates air heated by an electric heater through the packed bed, transferring heat to the solid storage material. In idle mode, the system remains on standby with minimal heat loss. During discharging, when electricity is needed, cooler air flows through the packed bed, absorbing the stored heat. This heated air then transfers its energy to a water-based Rankine cycle via an HRSG. The configuration of the system is shown in Figure 3.1.

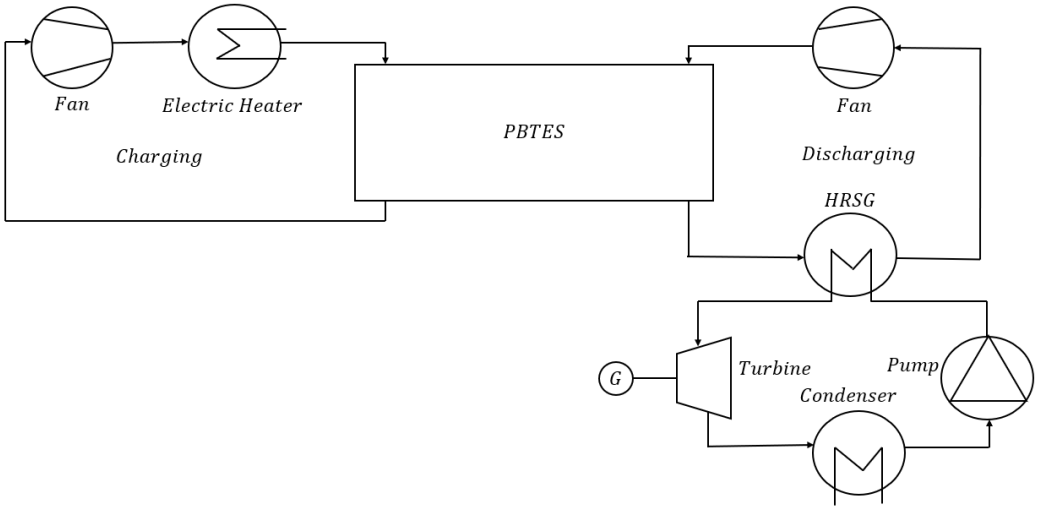

Figure 3.1: Schematic of the system including the PBTES during charging and discharging including the HRSG, combined Rankine cycle and auxilluary components for operation including a fan and electric heater.

The following sections consider the modelling of each system component, including their involvement during charging and discharging.

3.1.1 Numerical Model

The numerical model of the PBTES is based on a transient one-dimensional two-phase numerical model with including heat transfer mechanisms. The primary objective of the numerical model is to investigate the temperature distribution throughout the bed, mainly during charge and discharge.

Several assumptions are incorporated in the numerical model, including that the solid storage material consists of spherical rock particles, although in practice, the particles vary in shape and size. The air is treated as dry air, with moisture effects neglected along the length of the bed. Airflow is assumed to be uniform across the cross-sectional area, ignoring lateral mixing and resulting in a uniform temperature distribution perpendicular to the flow direction. To assess whether the temperature within each solid particle can be assumed uniform, the Biot number (Bi) is used. When Bi < 0.1, internal thermal resistance is negligible compared to surface resistance, justifying the assumption of a uniform particle temperature. The Biot number for the numerical model is defined and calculated in Appendix A.1. Additionally, in Figure A.1 in Appendix A.1, the Biot number is shown to be ranging from approximately 0.08 to 0.2 for particle diameters between 35 mm and 60 mm. Based on this, a uniform internal temperature is assumed for the particles in this numerical model. However, it should be noted that this assumption is most valid for particles up to 35 mm in diameter, while larger particles may exhibit internal temperature gradients. The dominant heat transfer mechanism is forced convection between the air and solid particles. For simplicity, radiative heat loss from the bed's outer surface and natural convection within the bed are neglected. Conduction between the air and solid particles is also ignored, as it is minor compared to the convective heat transfer under the assumed flow conditions.

The numerical model is inspired by the packed bed model developed by [Schumann, 1929]. This is based on a two-phase one-dimensional governing equation, which enables calculation of the time evolution and spatial distribution of both solid and fluid temperature along the bed. These equations are defined in 3.1 and 3.2.

$$\varepsilon \cdot \rho_F \cdot c_{p,F} \cdot \frac{\partial T_F}{\partial t} + \varepsilon \cdot \rho_F \cdot c_{p,F} \cdot \frac{\dot{m}_{air}}{\rho_F \cdot A_c \cdot \varepsilon} \cdot \frac{\partial T_F}{\partial z} = h \cdot A_s \cdot (T_S - T_F) - \frac{T_F - T_\infty}{R_{wall}} \tag{3.1}$$

$$(1 - \varepsilon) \cdot \rho_S \cdot c_{p,S} \cdot \frac{\partial T_S}{\partial t} = h \cdot A_s \cdot (T_S - T_F) \tag{3.2}$$

where T is the temperature, ρ is the density, c_p is the specific heat capacity. The subscripts F and S refer to the fluid (air) and solid phases, respectively. The term ε denotes the void fraction of the packed bed, while h is the convective heat transfer coefficient between the fluid and the solid, A_s represent the heat transfer surface area, and A_c is the cross-sectional area of the packed bed. $\dot{m}_{air}$ represents the mass flow rate of air, and T_∞ is the ambient temperature. The term R_{wall} represents the thermal resistance through the bed wall, which is presented in Section 3.1.2. The two-phase equations for the solid and fluid temperatures are discretized using first-order finite difference approximations. The time deriatives involving $\frac{\partial T_F}{\partial t}$ and $\frac{\partial T_S}{\partial t}$ is discretized using a forward explicit Euler scheme, whereas the spatial deriative involving $\frac{\partial T_F}{\partial z}$ is discretized using a first-order backward difference scheme. Specifically, an explicit time-stepping scheme is employed where the

temperature at the next time step is determined from known values at the current time step. The resulting discretized forms of the governing equations for the fluid and solid temperatures are shown in Equations 3.3 and 3.4.

$$T_{F,i}^{j+1} = T_{F,i}^{j} + \Delta t \cdot \left(\frac{h \cdot A_s \cdot (T_{S,i}^{j} - T_{F,i}^{j})}{\varepsilon \cdot \rho_F \cdot c_{p,F}} - \frac{\dot{m}_{\text{air}}}{\rho_F \cdot A_c \cdot \varepsilon} \cdot \frac{(T_{F,i}^{j} - T_{S,i}^{j})}{\Delta z} - \frac{1}{\varepsilon \cdot \rho_F \cdot c_{p,F}} \cdot \frac{T_{F,i}^{j} - T_{\infty}}{R_{wall} \cdot A_c \cdot \Delta z} \right) \tag{3.3}$$

$$T_{S,i}^{j+1} = T_{S,i}^{j} + \Delta t \cdot \left(\frac{h \cdot A_s \cdot (T_{F,i}^{j} - T_{S,i}^{j})}{(1-\varepsilon) \cdot \rho_S \cdot c_{p,S}} \right) \tag{3.4}$$

Where i indicates the current node, j represents the current time step, and $j+1$ represents the following time step. To discretize the numerical model, the domain is divided into control volumes based on the bed length L and the number of nodes N, as shown in Equation 3.5

$$\Delta z = \frac{L}{N} \tag{3.5}$$

The packed bed is modelled as a cylindrical bed divided into multiple layers along its length. Figure 3.2 illustrates the one-dimensional discretization, including the arrangement of solid storage material, insulation, and flow direction.

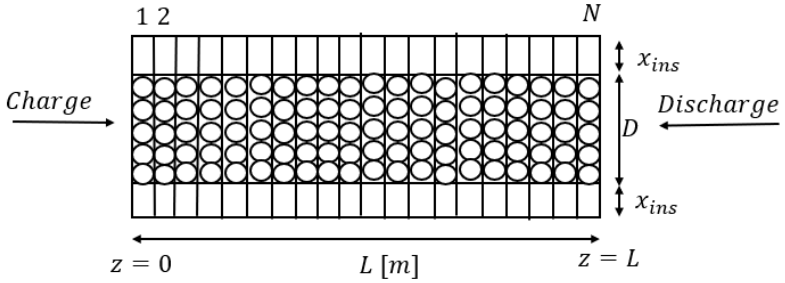

Figure 3.2: Schematic diagram of the packed bed with length L and N numer of elements. This is filled with spherical particles. The arrow indicates that is charged from left to right and discharged from right to left. The packed bed includes insulation around the cylinder.

The arrows indicate the flow direction in either charge or discharge mode. In charging mode, hot air flows from left to right. In discharging mode, cold air flows from right to left. As the transient temperature variation is based on the explicit scheme, a stability criterion is involved. The explicit method is conditionally stable, so to avoid numerical divergence, the following equation is implemented in the numerical model according to [Versteeg and Malalasekera, 2007]

$$\frac{\alpha \cdot \Delta t}{\Delta z^2} \leq \frac{1}{2} \tag{3.6}$$

Here α represents the thermal diffusivity of the solid material, Δt is the timestep, and Δz is the spatial discretisation. To solve the energy equations for both fluid and solid phases, appropriate boundary and initial conditions are applied consistently during both charging and discharging. These are applied consistently during the charge and discharge cycles

of the packed bed model. The domain is discretized in space and time using the finite difference approach, as illustrated in Figure 3.3.

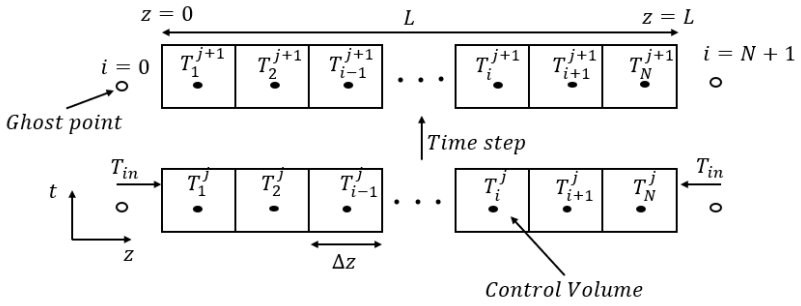

Figure 3.3: Discretized domain including the control volumes of the packed bed cylinder in space and time. This includes N number of nodes and two additional ghost points at the boundaries.

The spatial domain is divided into N control volumes, labelled $i = 1, 2, ...N$, with two additional ghost nodes at $i = 0$ and $i = N + 1$ used to implement the gradient boundary conditions. Time is discretized into time steps indexed by j, and the temperature at each spatial node and time step is denoted T_i^j indicating the value at node i and time step j. The air inlet temperature T_{in} is applied at the appropriate boundary depending on the flow direction. In charging mode, where the flow is from left to right, T_{in} is applied at $z = 0$. In discharging mode, where the flow is from right to left, T_{in} is applied at $z = L$. At both ends of the packed bed, the temperature gradient in the axial direction is set to zero. This means that at the first node, the gradient becomes

$$\frac{T_{S,1} - T_{S,0}}{\Delta z} = 0 \tag{3.7}$$

And at the final node, it becomes:

$$\frac{T_{S,N+1} - T_{S,N}}{\Delta z} = 0 \tag{3.8}$$

Initial temperatures for both the fluid and solid are specified uniformly across all nodes at the beginning of the simulation. A full summary of the boundary and initial conditions used in the numerical model can be found in Table A.1 in Appendix A.2.
The convection of air through the bed includes the heat transfer coefficient h, which is calculated using the Nusselt number as follows:

$$h = \frac{Nu \cdot k_{air}}{L_c} \tag{3.9}$$

Where k_{air} is the thermal conductivity of air, and L_c is the characteristic length. To determine the Nusselt number, both the Reynolds number, Re and the Prandtl number, Pr, must be found. The Reynolds number is determined using the velocity of the fluid, the characteristic length, which is determined based on the flow through the void space, which represents the portion of the packed bed occupied by the fluid and the kinematic viscosity. This is shown in Equation 3.10

$$Re = \frac{V_{air} \cdot L_c}{\nu_{air}} \tag{3.10}$$

Here, the characteristic length is determined based on the volume and area of the solid particle sphere and the void fraction. This is expressed in Equation 3.11

$$L_c = \left(\frac{6 \cdot V_{sphere}}{A_{sphere}}\right) \cdot \left(\frac{\varepsilon}{1-\varepsilon}\right) \tag{3.11}$$

The actual velocity of the fluid inside the bed is defined based on the superficial velocity and the void fraction shown in Equation 3.12

$$V_{air} = \frac{V_{air,s}}{\varepsilon} \tag{3.12}$$

Where the superficial velocity is the fluid's velocity if no solid material were present, this is based on the volumetric flow rate divided by the cross-sectional area of the packed bed. The void fraction is defined as the ratio of the volume of the gaseous phase occupied in the bed to the total volume of the bed. This is shown in Equation 3.13 according to [Springer, 2006]

$$\varepsilon = \frac{V_{void}}{V_{total}} \tag{3.13}$$

The Nusselt number represents the ratio of the convective to conductive heat transfer. For air flowing through a packed bed of spheres, an empirical correlation can be used to estimate the Nusselt number based on the Reynolds number and Prandtl number. One widely used correlation, valid in the range $22 \leq Re \leq 8,000$, provides an accuracy of $\pm$ 25%. This is defined in Equation 3.14

$$Nu_{forced} = (0.5 \cdot Re^{1/2} + 0.2 \cdot Re^{2/3}) \cdot Pr^{1/3} \tag{3.14}$$

The Prandtl number is calculated based on the thermophysical properties of air, evaluated at the mean temperature, which is taken as the arithmetic average of the inlet and outlet air temperatures in the bed.

3.1.2 Thermal Losses

To account for thermal losses to the surroundings, heat loss through the lateral surface of the packed bed TES cylinder is included in the numerical model. The top and bottom surfaces are assumed to be well insulated, and thus their heat loss is neglected. To minimize thermal losses, the cylinder is surrounded by two layers of insulation according to [von der Heyde, 2022]. Insulation involving aerated concrete and rock wool is used to reduce thermal losses. The packed bed cylinder, including the insulation, is illustrated in Figure 3.4

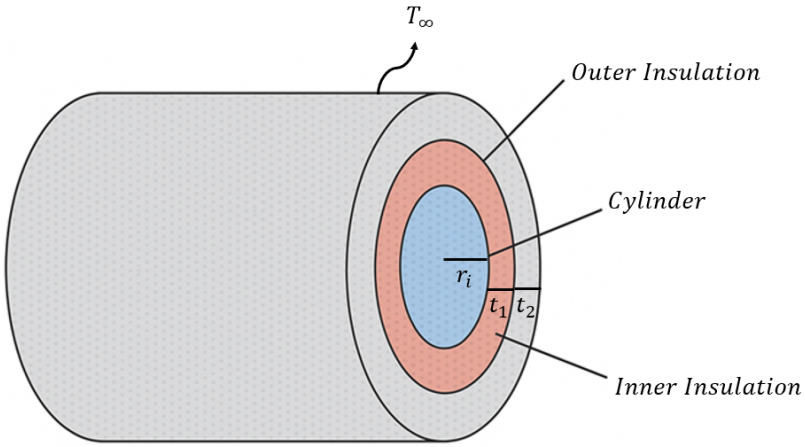

Figure 3.4: Schematic of the packed bed cylinder including the two layer of insulation, each associated with a thickness t_1 and t_2.

As defined in Equation 3.1, the heat loss to the surroundings is found using the thermal resistance through the wall R_{wall} and the temperature difference between the fluid and the ambient air. To determine the R_{wall}, it is based on a simple thermal resistance network approach, which includes radial conduction through the insulation layers and external convective heat transfer to ambient air. This is defined in Equation 3.15 [Cengel et al., 2017]

$$R_{\text{wall}} = \frac{\ln(r_1/r_i)}{2\pi \cdot L \cdot k_1} + \frac{\ln(r_2/r_1)}{2\pi \cdot L \cdot k_2} + \frac{1}{h_o \cdot 2\pi \cdot r_2 \cdot L} \tag{3.15}$$

Here L is the length of the bed, h_o is the convective heat transfer coefficient at the outer surface whose value is chosen to be 20 $W/(m^2 \cdot K)$ according to [von der Heyde, 2022], k_1, k_2 are the thermal conductivities of the inner and outer insulation layers used based on values provided by [von der Heyde, 2022], r_1 and r_2 are the outer radii after the inner and outer insulation layers, respectively. r_i is the inner radius of the cylinder. Note that internal convective resistance is not included here due to the assumption that the inner packed bed flow is sufficiently mixed or dominated by internal processes. The geometric and thermal properties used to obtain R_{wall} to determine the heat loss in the numerical model are listed in Table 3.1. These values reflect a configuration with two insulation layers, each 0.5 m thick, as proposed in the system by [von der Heyde, 2022].

Parameter	Value
D_i	9.44 m
r_i	4.72 m
r_1	0.5 m
r_2	0.5 m
k_1	0.13 W/(m·K)
k_2	0.39 W/(m·K)
h_o	20 W/(m²·K)
R_{wall}	0,00282 K/W

Table 3.1: Applied and calculated parameters for the heat losses in the PBTES numerical model.

3.1.3 Pressure Loss in Packed Bed

The pressure loss in the packed bed is considered, which involves the friction losses through the packed bed, which is calculated using the Ergun equation. Additionally, a pressure gradient associated with acceleration effects resulting from changes in fluid density is also implemented. Gravitational effects are neglected in this analysis, as the bed is assumed to have no elevation change. This is expressed in Equation 3.16 according to [Springer, 2006].

$$\frac{\Delta P}{L} = 1.75 \cdot \left(\frac{1-\varepsilon}{\varepsilon^3}\right) \cdot \frac{G^2}{\rho_F \cdot d_p} + 150 \cdot \left(\frac{(1-\varepsilon)^2}{\varepsilon^3}\right) \cdot \frac{G \cdot \mu_F}{\rho_F \cdot d_p^2} + \frac{G^2}{2} \cdot \left(\frac{1}{\rho_{\text{out}}} - \frac{1}{\rho_{\text{in}}}\right) \tag{3.16}$$

Where ΔP represents the pressure difference, L is the length of the bed, ε is the void fraction of the bed, and G is the mass flux of the fluid. The first two terms constitute the Ergun equation, which quantifies frictional pressure losses due to viscous and inertial interactions within the porous medium. The third term represents the pressure gradient associated with fluid acceleration resulting from density variation. The empirical coefficients 1.75 and 150 are widely accepted constants that provide good agreement with experimental data for a wide range of Reynolds numbers.

3.2 Heat Recovery Steam Generator

The HRSG operates during discharge of the PBTES, utilizing the heated air extracted from the bed. The discharge temperature of the air serves as the inlet temperature to the HRSG, where air functions as the hot fluid and water/steam as the cold fluid. On the cold side, water and steam flow through three sequential heat exchanger sections: the economizer, evaporator, and superheater. The configuration of the HRSG is illustrated in Figure 3.5.

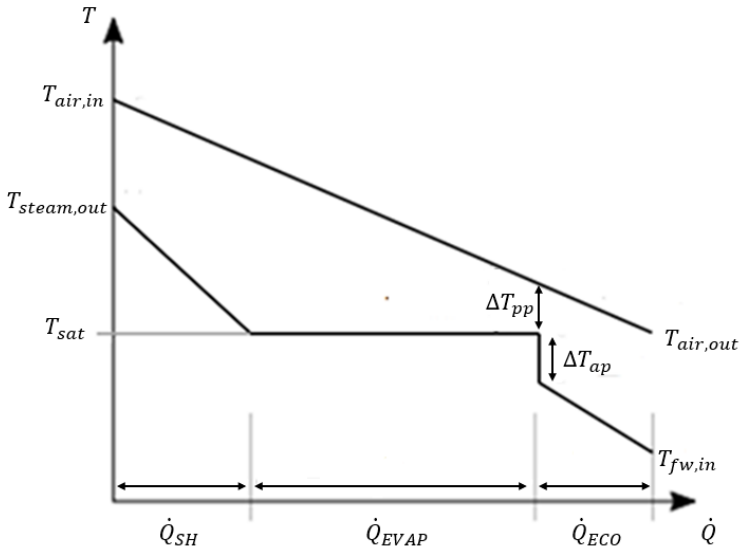

Figure 3.5: Temperature profiles of air and water within the HRSG, showing key inlet and outlet temperatures. The heat transfer process is divided into three regions: superheater (1), evaporator (2) and economizer (3). This includes the ΔT_{pp} and ΔT_{ap} representing the pinch point and approach temperature difference.

The HRSG includes the pinch point temperature difference as the minimum temperature difference between the steam saturation and the evaporator air outlet temperature, where the pinch point temperature difference affects the required heat transfer area. By lowering the pinch point, the steam production can be increased, however, this comes with a cost of increasing the heat transfer area required, which can be seen in Figure A.2 in Appendix A.3. A suitable pinch point temperature difference in the HRSG is therefore chosen to be 10 K. Furthermore, the approach temperature difference is implemented between the steam saturation temperature and the economizer water outlet temperature, which is chosen to be 5 K according to [von der Heyde, 2022]. The mass flow rate of water-steam is determined using an energy balance between the heated air and the superheater and evaporator, as the air mass flow rate, pressure, and temperature are known. The energy balance for the HRSG is shown in Equation 3.17.

$$\dot{Q}_{HRSG} = \dot{m}_{water} \cdot (h_{steam,out} - h_{fw}) = \dot{m}_{air} \cdot (h_{air,in} - h_{air,out}) \tag{3.17}$$

By assuming that the mass flow rate through the economizer is equal to that through the evaporator and superheater, the heat transfer rate can be determined. Subsequently, an energy balance can be used to calculate the temperature of the cooled air exiting the HRSG. The heat transfer rate involving the economizer, evaporator and superheater is calculated through the enthalpy difference and mass flow of water-steam, which is defined in Equation 3.18, 3.19 and 3.20.

$$\dot{Q}_{eco} = \dot{m}_{water} \cdot (h_{eco,out} - h_{fw}) \tag{3.18}$$

$$\dot{Q}_{evaporator} = \dot{m}_{water} \cdot \Delta h_{fg} + \dot{m}_{water} \cdot (h_{sat,water} - h_{eco,out}) \tag{3.19}$$

$$\dot{Q}_{superheater} = \dot{m}_{water} \cdot (h_{steam,out} - h_{sat,vapor}) \tag{3.20}$$

Where Δh_{fg} represent the latent heat of vaporization. The total heat transfer surface area of the HRSG, is calculated using the heat transfer rate, the overall heat transfer coefficient U and the *Log Mean Temperature Difference* (LMTD), which is shown in Equation 3.21.

$$A_{HRSG} = \frac{\dot{Q}_{HRSG}}{U \cdot LMTD} \tag{3.21}$$

The heat transfer rate in the HRSG is obtained by summing the heat transfer rate in the economizer, evaporator and superheater. The overall heat transfer coefficient U is defined in each heat exchanger in the HRSG, whose values are defined in Section 4.2. The LMTD method accounts for the temperature difference between the hot and cold fluids at both ends of the heat exchanger, defined as:

$$LMTD = \frac{\Delta T_1 - \Delta T_2}{\ln(\Delta T_1 / \Delta T_2)} \tag{3.22}$$

Where ΔT_1 and ΔT_2 represent the temperature difference for the hot and cold fluid in the HRSG.

This is defined in Equation 3.23 and 3.24

$$\Delta T_1 = T_{h,out} - T_{c,in} \tag{3.23}$$

$$\Delta T_2 = T_{h,in} - T_{c,out} \tag{3.24}$$

Figure 3.6 illustrates the temperature differences involved in the LMTD method in a counter-current heat exchanger.

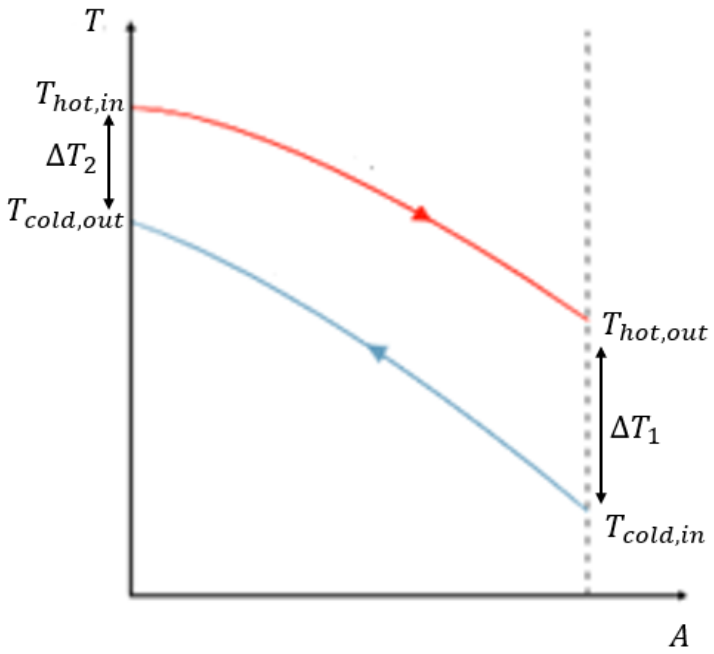

Figure 3.6: Illustration of the LMTD method in a counter-current heat exchanger including the hot and cold fluid temperature entering and leaving the heat exchanger.

The HRSG will be further explored in the following section in relation to the Rankine Cycle.

3.3 Rankine Cycle

The Rankine Cycle is one of the most well-known power production techniques nowadays and is implemented worldwide. It is a thermodynamic cycle primarily used in steam power plants to generate electricity. The cycle is shown in a T-s diagram in Figure 3.7.

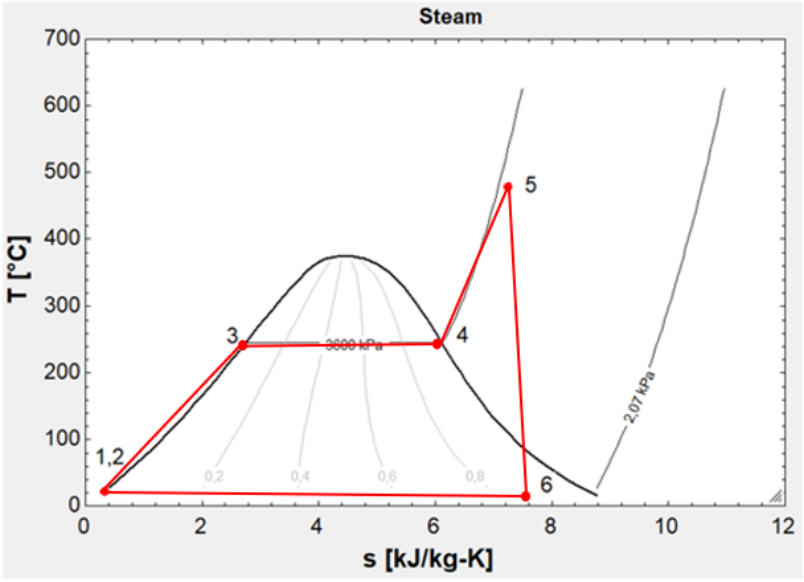

Figure 3.7: T-s diagram for a basic steam Rankine cycle.

The process involves the feedwater pump that pressurizes the water to the pressure in the HRSG. The water is heated up to the saturation temperature, which afterwards goes through evaporation. The steam is then superheated to the desired steam temperature. This occurs in the HRSG through an isobaric process. The steam is then expanded through the turbine to convert into usable power, where the temperature in most practical applications is dropped below the saturation curve. The saturated vapour is then condensed at constant pressure and temperature, and the cycle repeats.

The pump and turbine are both modelled in the Rankine cycle based on a specified pump and turbine efficiency. The actual power generated or consumed is determined by their efficiencies, as expressed in Equations 3.25 and 3.26:

$$\dot{W}_{pump} = \frac{\dot{m}_{water} \cdot (h_2 - h_1)}{\eta_{pump}} \tag{3.25}$$

$$\dot{W}_{turbine} = \dot{m}_{water} \cdot (h_5 - h_6) \cdot \eta_{turbine} \tag{3.26}$$

The condenser is responsible for cooling the steam discharged from the turbine, which is modelled similarly to the HRSG. The water-steam from the turbine outlet serves as the hot fluid, while water from an external source, such as a cooling tower, acts as the cold fluid. The heat transfer rate involving the condenser can be calculated through the enthalpy difference and mass flow of the water-steam, defined in Equation 3.27

$$\dot{Q}_{condenser} = \dot{m}_{water} \cdot (h_6 - h_1) \tag{3.27}$$

The condenser also uses the LMTD to determine the heating surface area, with a similar approach to the HRSG explained earlier, including the temperature difference between the hot and cold fluid. The overall efficiency of the Rankine Cycle is calculated as the ratio of net work output to the heat input provided by the HRSG, as defined in Equation 3.28:

$$\eta_{RK} = \frac{\dot{W}_{net}}{\dot{Q}_{in}} = \frac{\dot{W}_{turbine} - \dot{W}_{pump}}{\dot{Q}_{HRSG}} \tag{3.28}$$

Where W_{net} represents the net power generated, which is the difference between the turbine power output and the power consumed by the pump. Two configurations are considered for the Rankine cycle in this thesis, involving a SP and DP cycle, which will be explored in the following section.

3.3.1 Single Pressure Rankine Cycle

The *Single-Pressure* (SP) Rankine Cycle configuration applied in this thesis is illustrated in Figure 3.8

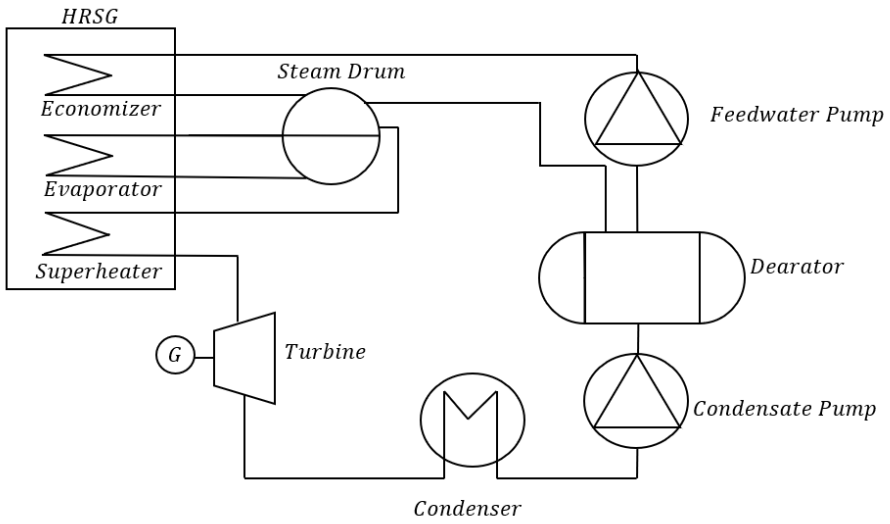

Figure 3.8: Schematic diagram a SP Rankine cycle including the HRSG, turbine, condenser, pumps and dearator. The HRSG consists of an economizer, evaporator, and superheater, all connected to a steam drum.

This configuration includes the three different heat exchangers in the HRSG, the economizer, evaporator and superheater. Initially, the water enters the economizer where it is preheated to the approach temperature. After the economizer it enters the steam drum, which acts as a reservoir that separates the water and steam. The water is fed into the evaporator, where it is heated until it evaporates before entering the drum once again. The saturated steam is then led into the superheater, where it is further heated to a superheated vapor. The superheated steam expands through the turbine, generating mechanical work that is subsequently converted into electricity. A deaerator is also implemented in the cycle. The deaerator serves two main purposes; the primary purpose is to remove dissolved gases, including oxygen, from the feedwater to prevent corrosion, and the secondary purpose is to preheat the feedwater using steam extracted from the evaporator.

The SP Rankine cycle is used to investigate the tendencies and effects of adjusting parameters such as the pressure in relation to the specific work of the turbine and thermal efficiency. The influence of the HRSG operating pressure on the Rankine cycle performance is illustrated in Figures 3.9 and 3.10. Figure 3.9 shows the variation in specific work

output from the turbine as a function of the HRSG pressure, while Figure 3.10 presents the corresponding thermal efficiency of the cycle.

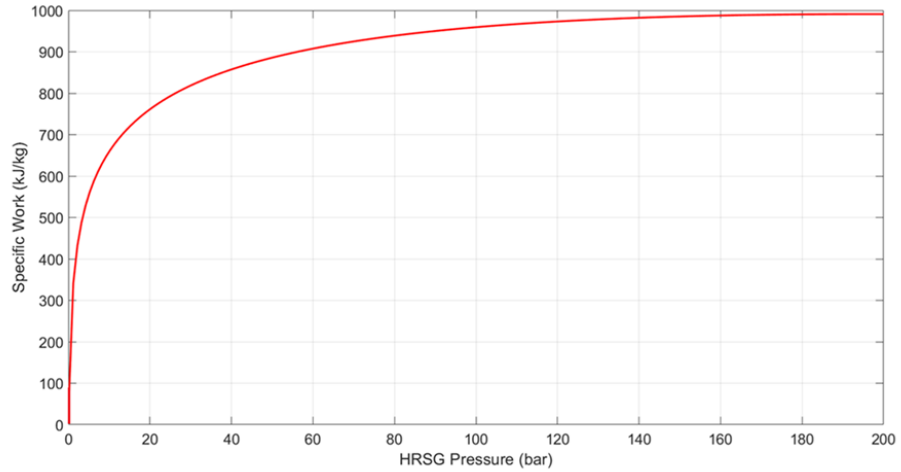

Figure 3.9: The turbine specific work as a function of the HRSG pressure for the single pressure Rankine cycle.

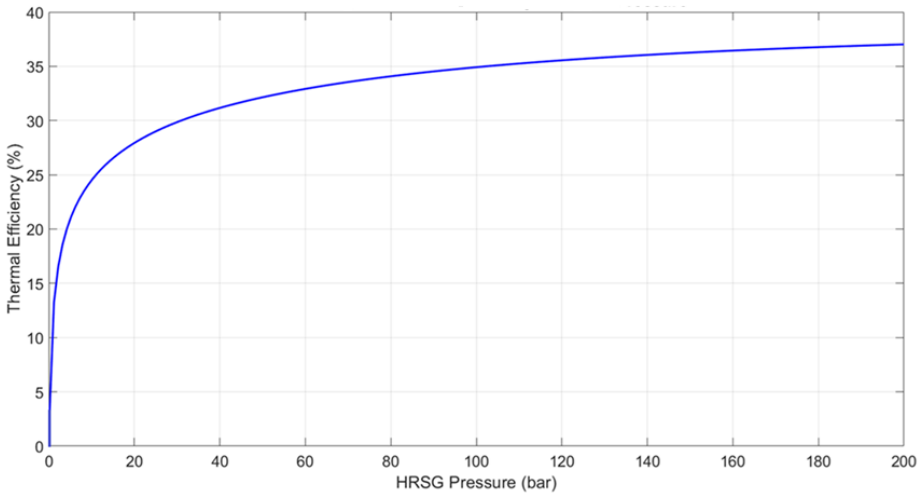

Figure 3.10: The thermal efficiency as a function of the HRSG pressure for the single pressure Rankine cycle.

As HRSG pressure increases, the saturation and superheat temperatures of steam rise, which leads to a higher enthalpy drop across the turbine and thus greater specific work output. This also improves thermal efficiency, as a larger fraction of the input heat is converted to useful work. The specific work initially increases significantly with pressure, but the rate of increase diminishes at higher pressures. While increasing the HRSG pressure in a SP Rankine cycle improves both the specific work output and thermal efficiency, further enhancement of cycle performance can be achieved through alternative configurations. One such approach is the DP Rankine cycle, which is commonly used to increase energy recovery and overall efficiency. This configuration is examined in the following section.

3.3.2 Dual Pressure Rankine Cycle

There are different combinations of the superheater, evaporator and economizer in the HRSG. Among these configurations, the DP Rankine cycle offers a potential advantage by incorporating two pressure levels, thereby enabling more effective utilization of the thermal energy available from the hot air stream. The configuration of the dual-pressure Rankine cycle is illustrated in Figure 3.11

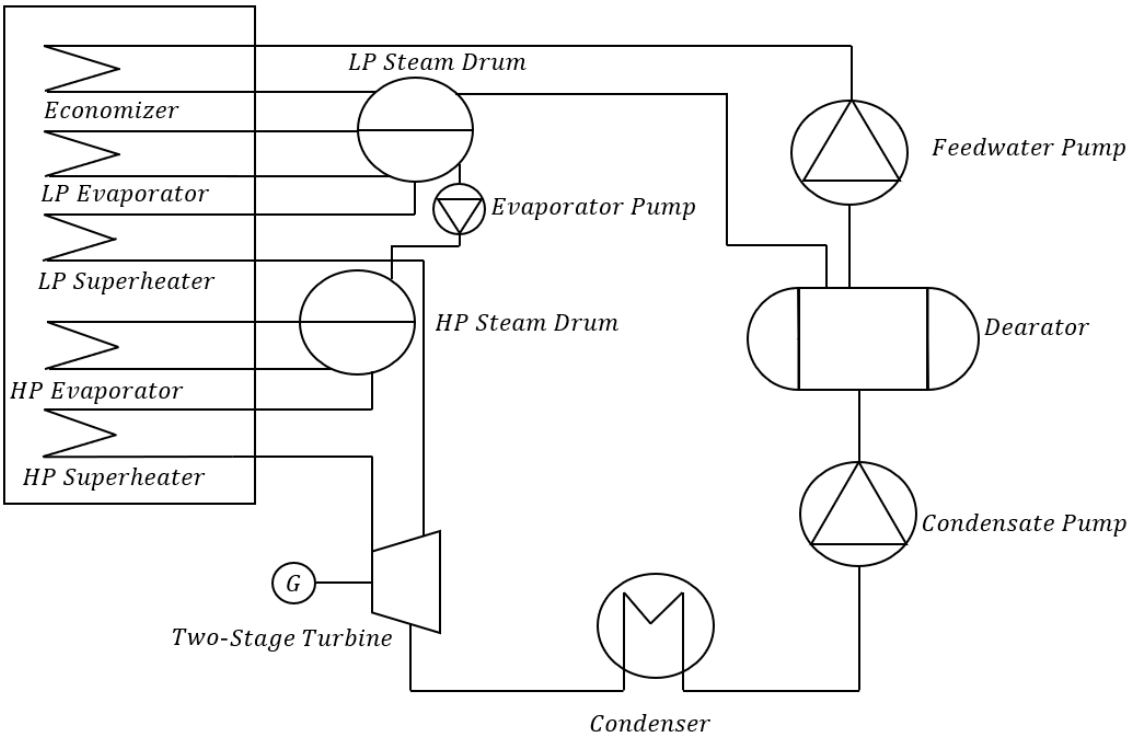

Figure 3.11: Schematic diagram of the DP Rankine cycle including the HRSG, turbine, condenser, pumps and dearator. The HRSG consists of an economizer, LP evaporator, LP superheater, HP evaporator and HP superheater, all connected to a LP and HP steam drum.

The DP cycle operates similarly to a SP Rankine cycle but includes a distinct *Low-Pressure* (LP) and *High-Pressure* (HP) part. The LP part comprises an LP economizer, LP evaporator, LP steam drum, and LP superheater. The HP part includes an HP evaporator, HP steam drum, and HP superheater although the economizer is excluded. It is assumed that the saturated water from the LP evaporator is being heated up in the HP evaporator. Steam generated in both the LP and HP superheaters is expanded through a shared turbine, modelled as a two-stage expansion process. In practice, this would require a multistage turbine, a point that is discussed in more detail in Section 6.

The pressure involving 67 bar for the SP Rankine cycle is chosen equivalent to the operating pressure by [von der Heyde, 2022]. The 20 bar utilized in the DP cycle is used as an initial reference for the cycle, which will be further investigated throughout the thesis. This LP level in a DP Rankine cycle is also suitable, as it provides a sufficient balance between efficient heat recovery and thermal efficiency. The parameters utilized in the SP and DP Rankine cycle model are presented in Table 3.2.

Parameters	SP	DP
$P_{HP}\,[bar]$	67	67
$P_{LP}\,[bar]$	-	20
$T_{air,in}\,[°C]$	650	650
$T_{condenser}\,[°C]$	50	50
$P_{condenser}\,[bar]$	0,12	0,12
$T_{LP,steam,out}\,[°C]$	-	273
$T_{HP,steam,out}\,[°C]$	480	480
$T_{feedwater}\,[°C]$	105	105
$\Delta T_{pp}\,[K]$	10	10
$\Delta T_{approach}\,[K]$	5	5
$\eta_{turbine}\,[\%]$	93	93
$\eta_{pump}\,[\%]$	85	85

Table 3.2: Summarised values utilized in the DP and SP Rankine cycle.

The corresponding results for the SP and DP cycle configurations are further examined in Section 4.2.

3.4 Performance Metrics of the Packed TES and Rankine Cycle System

Several key parameters are used to describe the performance of both the packed TES and the integrated Rankine cycle. These include energy balances for the electric heater and fan, as well as charging, discharging, and system-level efficiencies. The charging efficiency of the packed bed quantifies how effectively electrical energy input is converted into stored thermal energy in the solid bed material. It is defined as the ratio of thermal energy stored during the charging period to the total electrical energy consumed by the heater and fan, defined in Equation 3.29.

$$\eta_{charge} = \frac{E_{stored}}{E_{fan} + E_{heater}} \tag{3.29}$$

Here E_{heater} and E_{fan} denote the electrical energy consumed by the heater and fan, respectively, as defined in Equations 3.31 and 3.35. The stored thermal energy E_{stored} is defined in Equation 3.30.

$$E_{stored} = (1-\varepsilon) \cdot \rho_S \cdot V_{bed} \cdot c_{p,S} \cdot \left(T_{final} - T_{initial}\right) \tag{3.30}$$

The value of specific heat capacity is used for the solid material according to [von der Heyde, 2022] as shown in Table 1.2

$$E_{heater} = \dot{m}_{air} \cdot (h_{air,bed} - h_{air,fan}) \cdot \Delta t_{charge} \tag{3.31}$$

$$E_{fan,charge} = \frac{\Delta P \cdot \dot{m}_{air} \cdot \Delta t_{charge}}{\rho_F \cdot \eta_{fan}} \tag{3.32}$$

Similarly, the discharging efficiency reflects how much of the stored thermal energy is recovered and delivered to the HRSG, considering the fan power consumption during discharge. This is expressed in Equation 3.33.

$$\eta_{discharge} = \frac{E_{recovered}}{E_{stored} + E_{fan,discharge}} \tag{3.33}$$

Here $E_{recovered}$ represents the thermal energy delivered to the HRSG during discharge, and $E_{fan,discharge}$ denotes the electrical energy consumed by the fan. These are defined in Equations 3.34 and 3.35, respectively.

$$E_{recovered} = \dot{m}_{air} \cdot (h_{air,in} - h_{air,out}) \cdot \Delta t_{discharge} \tag{3.34}$$

$$E_{fan,discharge} = \frac{\Delta P \cdot \dot{m}_{air} \cdot \Delta t_{discharge}}{\rho_F \cdot \eta_{fan}} \tag{3.35}$$

The ρ_F represent the density of air, which is based on an arithmetic average temperature between the air inlet and outlet temperature of the bed. For the integrated PBTES and Rankine cycle, three key efficiency metrics are defined involving the power-to-heat, heat-to-power and power-to-power efficiencies. The power-to-heat efficiency is the ratio of useful thermal energy recovered from the HRSG during discharge, accounting for the electric energy used by the fan, to the total electric energy used for charging by the heater and the fan. It quantifies how effectively the system converts input electricity into usable heat. This is defined in Equation 3.36

$$\eta_{p2h} = \frac{\dot{Q}_{HRSG} - \frac{1}{\eta_{fan}} \cdot E_{fan,discharge}}{E_{fan,charge} + E_{heater}} \tag{3.36}$$

The heat-to-power efficiency is the ratio of the net electric work output in the Rankine cycle to the thermal energy rate recovered during discharge from the HRSG. This is defined in Equation 3.37

$$\eta_{h2p} = \frac{\dot{W}_{net}}{\dot{Q}_{HRSG}} \tag{3.37}$$

The power-to-power or round-trip efficiency of the combined system can thereby be determined as the product of these efficiencies. This efficiency tells how effectively the electrical energy used for charging is converted back into net electricity during discharging. This is defined in Equation 3.38

$$\eta_{p2p} = \eta_{p2h} \cdot \eta_{h2p} \tag{3.38}$$

With both the PBTES and the integrated Rankine cycle modelled, the next section presents the corresponding results.

Chapter 4

Verification and Results of the Packed Bed TES and Rankine Cycle

This chapter presents the results involved in the packed bed TES and attached Rankine cycle, including a verification of the system. The performance of both SP and DP Rankine cycle configurations is analyzed. In addition, key system parameters such as energy consumption, heat transfer rates, and temperature evolution over time and along the packed bed are evaluated to assess the overall performance of the system.

4.1 Verification of the Numerical Model

The packed bed thermal energy storage system, based on the existing ETES plant in Germany [von der Heyde, 2022], serves as the reference case for this thesis. The initial focus is on the PBTES. Table 4.1 summarizes the geometric and operational parameters used in the numerical model to evaluate temperature distribution and overall system behavior.

Parameters	**Model**
Volume of bed $[m^3]$	700
Length of bed $[m]$	10
Diameter of bed $[m]$	9,44
d_p $[m]$	0,035
ρ_S $[kg/m^3]$	2.730
$c_{p,S}$ $[J/(kg \cdot K)]$	1.100
ε $[-]$	0,47
T_{charge} $[°C]$	650
E_{stored} $[MWh]$	130
Air Pressure $[kPa]$	101,325
T_{amb} $[°C]$	20

Table 4.1: Input parameters used in the PBTES numerical model, adapted from the ETES plant specifications reported by [von der Heyde, 2022].

These parameters define the thermal storage bed's geometry and operating conditions during both charging and discharging cycles. The stored energy is calculated based on the thermal capacity of the solid material, as outlined in [von der Heyde, 2022]. The energy stored in the air is neglected due to its relatively minor contribution, with detailed calculations provided in Appendix A.4. Selected parameters will be varied in the sensitivity analysis in Section 5 to investigate their influence on thermal performance and temperature behavior within the bed.

Initially, the numerical model is verified using data from the PBTES system described by [von der Heyde, 2022], which employs a high-temperature, vertically oriented packed bed with volcanic rock as the storage medium. The verification is based on data from the ETES plant over a 24-hour operational period that includes both charging and discharging phases. The idle period between these phases is not modeled, under the assumption that the temperature remains constant during this time. The verification focuses on the temperature evolution over time and along different axial positions within the packed bed, as shown in Figures 4.1 and 4.2.

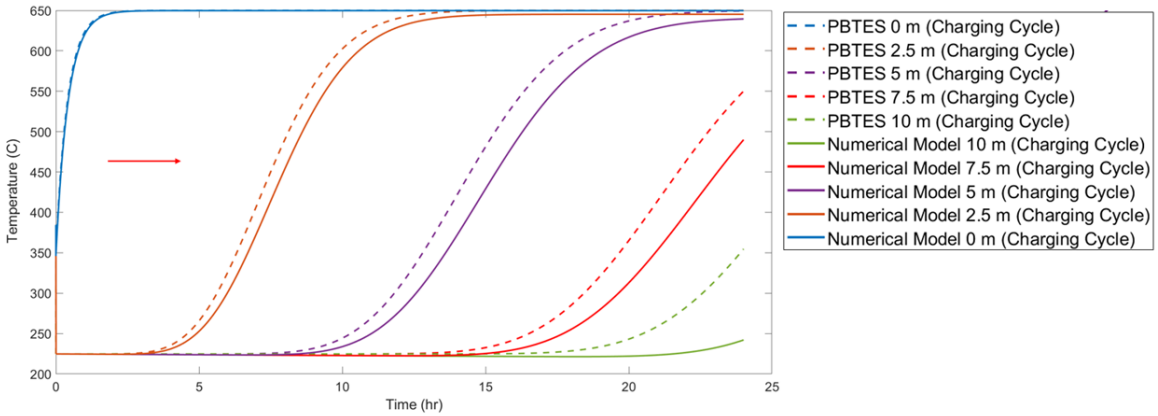

Figure 4.1: Temperature distribution for 24-hour charging operation of the numerical model and the PBTES by [von der Heyde, 2022]. The dash lines indicates the PBTES model by [von der Heyde, 2022] whereas the solid lines represent the numerical model. The arrow indicates the flow direction

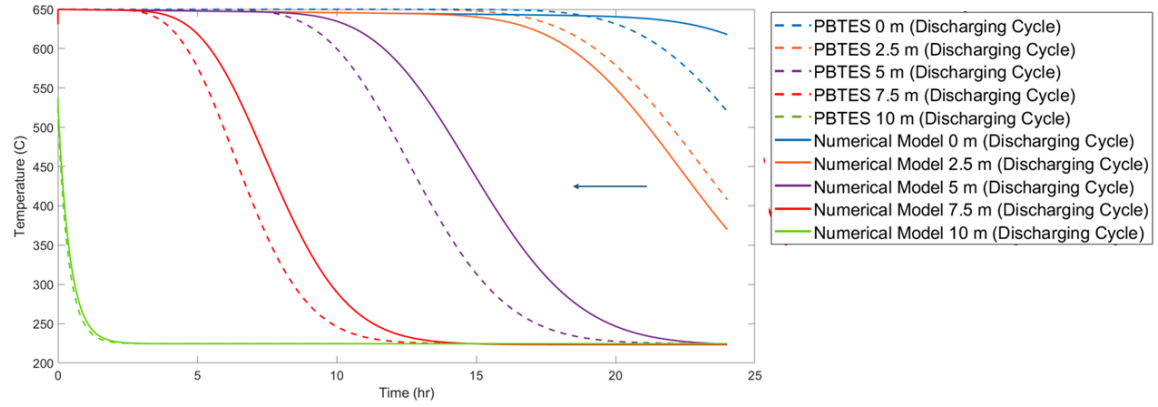

Figure 4.2: Temperature distribution for 24-hour discharging operation of the numerical model and the PBTES by [von der Heyde, 2022]. The dash lines indicates the PBTES model by [von der Heyde, 2022] whereas the solid lines represent the numerical model. The arrow indicates the flow direction

Figure 4.1 presents the fluid temperature as a function of time during the charging process for both the numerical model and the reference PBPTES model, evaluated at five distinct locations along the bed: 0.0 m, 2.5 m, 5.0 m, 7.5 m, and 10.0 m. The arrow on Figure 4.1 indicates the flow direction along the bed. The solid lines represent the numerical model, while the dashed lines correspond to the PBPTES reference data. Each curve indicates the fluid temperature at a specific position. The numerical model at the positions $z = 0\,m$ and $z = 2.5\,m$ closely matches the reference model. The temperature at these positions rises

sharply in the initial hours of charging and reaches the maximum temperature of approximately 650 °C. This agreement suggests that the numerical model accurately captures the heat transfer dynamics near the inlet of the bed, where the hot air is introduced. While the middle of the bed indicate trends are qualitatively similar, the numerical model exhibits a slightly delayed response compared to the reference. This discrepancy may be attributed to discretization errors or differences in how axial dispersion and thermal inertia are modeled. Even though the numerical model are assumed to be grid independent, utilizing 200 cells, which is shown in Figure A.3 in Appendix A.5. At the end of the bed, demonstrate the largest differences between the models. The reference model shows a more rapid and earlier increase in temperature, whereas the numerical model predicts a slower thermal response. These deviations are primarily due to model simplifications compared to the PBTES, including the heat losses, insulation and the neglect of radiative heat transfer. Additionally, the larger deviation could arise from the boundary condition assumptions in the numerical model. This will be further discussed in Section 6.

Figure 4.2 presents the fluid temperature as a function of time during the discharging process for both the numerical model and the reference PBPTES model, also evaluated at five distinct locations along the bed: 0.0 m, 2.5 m, 5.0 m, 7.5 m, and 10.0 m. The solid lines represent the numerical model, while the dashed lines correspond to the PBPTES reference data. Each curve indicates the fluid temperature at a specific position. The cold fluid enters the bed from the right indicated by the arrow in Figure 4.2 gradually propagating through the bed toward the end as heat is extracted. The temperature at the inlet of the bed drops rapidly at the beginning of the discharge process, while the temperature towards the end remains nearly constant at the initial value for a considerable duration before eventually declining. Overall, the numerical model shows good agreement with the PBTES model across the positions. However it can be observed that there is a higher deviation in the discharging mode compared to the charging mode. The curves align close at the inlet of the bed between the PBTES and the numerical model. A higher deviation between the numerical and benchmark models is noticeable along the bed. The benchmark model predicts an earlier temperature decline, while the numerical model exhibits a slightly delayed response. This may stem from differences in the numerical treatment of convective and dispersive heat transfer.

Figures 4.3 and 4.4 present the corresponding axial temperature distributions during the charging and discharging cycles.

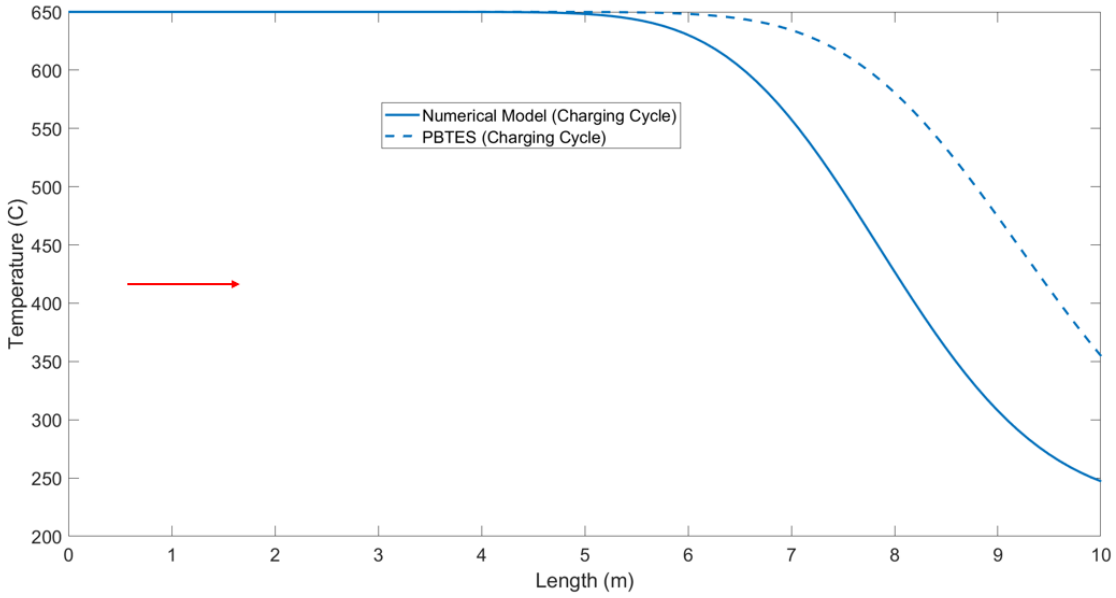

Figure 4.3: Temperature distribution across the length of the bed for 24-hour charging operation of the numerical model and the PBTES by [von der Heyde, 2022]. The dash lines indicates the PBTES model by [von der Heyde, 2022] whereas the solid lines represent the numerical model. The arrow indicates the flow direction

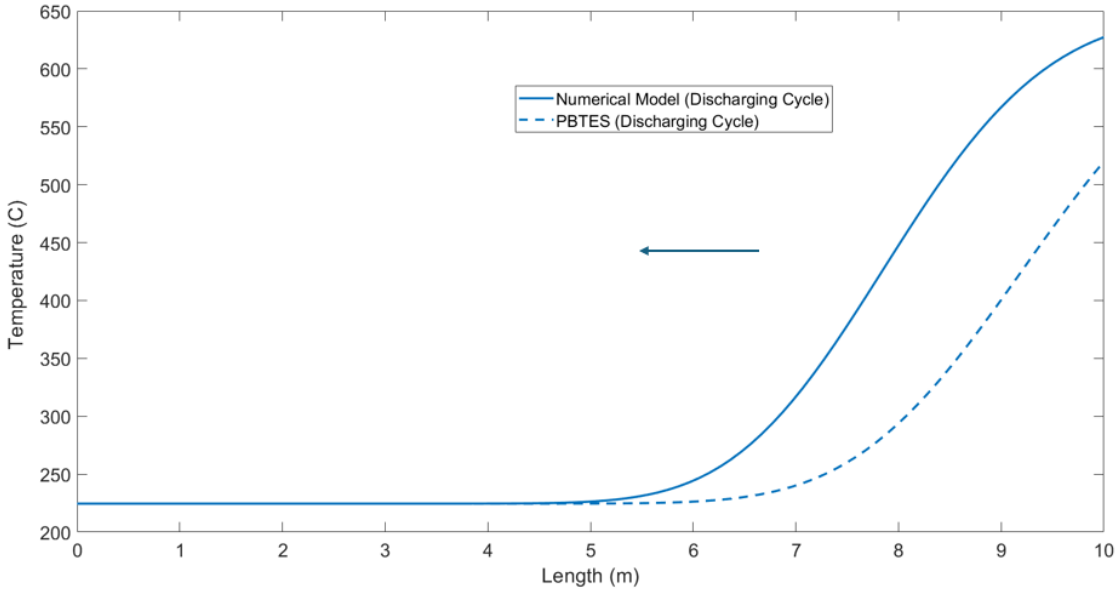

Figure 4.4: Temperature distribution across the length of the bed for 24-hour discharging operation of the numerical model and the PBTES by [von der Heyde, 2022]. The dash lines indicates the PBTES model by [von der Heyde, 2022] whereas the solid lines represent the numerical model. The arrow indicates the flow direction

Figure 4.3 illustrates the temperature distribution along the length of the bed for the numerical model and the PBTES data for the charging cycle. The solid line indicates the numerical model whereas the dash line represents the PBTES reference. In both models, the inlet region maintains a relatively high temperature. As the heat is provided through the bed over time the end of the bed is not sufficently heated up, leading to a decline in the temperature along the length of the bed. The numerical model exhibits a more gradual decline in temperature beyond approximately 5 meters, with the outlet temperature falling to around 250°C. In contrast, the PBTES model shows a similar general trend but with a slightly delayed and less steep decline in temperature. The thermal front in this model appears to propagate slightly further along the bed before significant temperature reduction occurs. The differences between the two curves can be attributed to the simplifications including the heat transfer mechanicms and implemented boundary conditions.

Figure 4.4 illustrates the temperature distribution along the length of the bed for the numerical model and the PBTES data for the discharging cycle. The solid line indicates the numerical model whereas the dash line represents the PBTES reference. During the discharging cycle, cold air is introduced into the bed at the inlet and it flows through the bed to extract thermal energy stored in the solid packing material. This results in a progressive decrease in the air temperature as it moves downstream, governed by convective heat transfer from the solid particles to the air. The temperature of air is high at the end of the bed and beyond approximately 5 meters, the temperature begins to decrease as the energy is extracted. The numerical model shows a sharper and more rapid temperature between 6 m and 10 m, eventually reaching an outlet temperature of around 620 °C. In contrast, the PBTES model reaches a lower outlet temperature of approximately 500 °C. This difference is mainly due to the difference in the simplifications assumed in both models.

Tables 4.2, 4.3, and 4.4 present the mean relative error and the coefficient of determination (R^2) for temperature evolution at various positions along the packed bed during both charging and discharging cycles. These error metrics assess the accuracy of the numerical model by comparing it with the results from the PBTES system described by [von der Heyde, 2022]. Additionally, the calculated mean relative error and R^2 value for the entire length of the packed bed during both cycles are provided, offering a broader perspective on the discrepancies between the numerical model and PBTES performance.

Charging	**0 m**	**2.5 m**	**5 m**	**7.5 m**	**10 m**
Mean Relative Error [%]	0,01	2,32	4,21	5,32	7,32
R^2 [-]	0,99	0,97	0,95	0,93	0,89

Table 4.2: Error metrics comparison between the numerical model and the PBTES by [von der Heyde, 2022] at different positions along the packed bed during charging cycle.

Discharging	**0 m**	**2.5 m**	**5 m**	**7.5 m**	**10 m**
Mean Relative Error [%]	6,74	5,63	14,43	7,32	0,03
R^2 [-]	0,87	0,95	0,78	0,93	0,98

Table 4.3: Error metrics comparison between the numerical model and the PBTES by [von der Heyde, 2022] at different positions along the packed bed during discharging cycle.

	Charging Cycle	**Discharging Cycle**
Mean Relative Error [%]	15,43	14,82
R^2 [-]	0,8	0,81

Table 4.4: Error metrics comparison between the numerical model and the PBTES by [von der Heyde, 2022] along the packed bed during charging and discharging cycle.

As shown in Table 4.2, the mean relative error during the charging cycle increases along the bed from 0.01% at the inlet (0 m) to 7.32% at the outlet (10 m), while the R^2 value decreases from 0.99 to 0.89. This indicates high accuracy near the inlet and increasing deviation along the bed, likely due to cumulative modeling errors. Table 4.3 presents a more irregular error distribution during the discharging cycle, with the highest error of 14.43% observed at 5 m and a sharp drop to 0.03% at 10 m. The R^2 values range from 0.78 to 0.98, suggesting variable model performance at different positions. Table 4.4 summarizes the overall performance along the bed for both cycles. The mean relative error is slightly higher for charging (15.43%) compared to discharging (14.82%), while the R^2 values are nearly identical (0.80 and 0.81), confirming that the numerical model generally captures the thermal dynamics, albeit with localized discrepancies.

Despite some discrepancies, a close agreement at the upper layers of the bed confirms that the numerical model correctly simulates the inlet-driven heat transfer during charging and discharging. The larger deviations towards the outlet suggest that the model could be improved by refining spatial discretization or enhancing the representation of heat transfer mechanisms. Despite these limitations, the model accurately captures the qualitative behavior of thermal front progression and overall heat transfer trends. These results support the model's validity and its applicability for further simulations and evaluations. A further performance comparison between the numerical model and the PBTES involves the power-to-heat, heat-to-power and power-to-power efficiency, including the energy requirement of the auxiliary components and estimated heat losses for both the numerical model and PBTES provided by [von der Heyde, 2022]. These parameters are shown involving the charging and discharging cycle of the 24-hour period in Table 4.5.

Combined system parameters	PBTES	Numerical Model
E_{in} $[MWh]$	120	117,36
$E_{released}$ $[MWh]$	112	104
$E_{fan,charge}$ $[MWh]$	2.4	2.4
$E_{fan,discharge}$ $[MWh]$	2.4	2.4
E_{heater} $[MWh]$	121	121
$Q_{loss,charge}$ $[MWh]$	7.05	12.93
$Q_{loss,discharge}$ $[MWh]$	7.05	12.93
η_{charge} $[\%]$	93	89
$\eta_{\text{discharge}}$ $[\%]$	92	89
η_{h2p} $[\%]$	28	26
η_{p2h} $[\%]$	91	87
η_{p2p} $[\%]$	25	23.5

Table 4.5: Applied and determined performance values for the numerical model and the PBTES by [von der Heyde, 2022].

The results show that the PBTES slightly outperforms the numerical model across most metrics, particularly in charging and discharging efficiency. The numerical model experiences higher heat losses, which reduce its overall performance. This may be attributed to simplified assumptions and less effective thermal insulation in the model. Nonetheless, the model provides a reasonable approximation and is suitable for further analysis.

4.2 Performance of the Rankine Cycle

The Rankine cycle is utilized during the discharge of the bed. Similar to the PBTES model, reference values from the ETES system described in [von der Heyde, 2022] are used where available. For parameters not provided, reasonable assumptions are applied which is provided in Table 3.2 for the SP and DP cycle. To simplify the analysis, heat losses from the packed bed during discharge are neglected, and the air temperature entering the HRSG is assumed to be uniform. The analysis begins with the SP Rankine cycle operating at 67 bar. Key values for pressure, mass flow rate, temperature, and specific enthalpy throughout the cycle are shown in Figure 4.5.

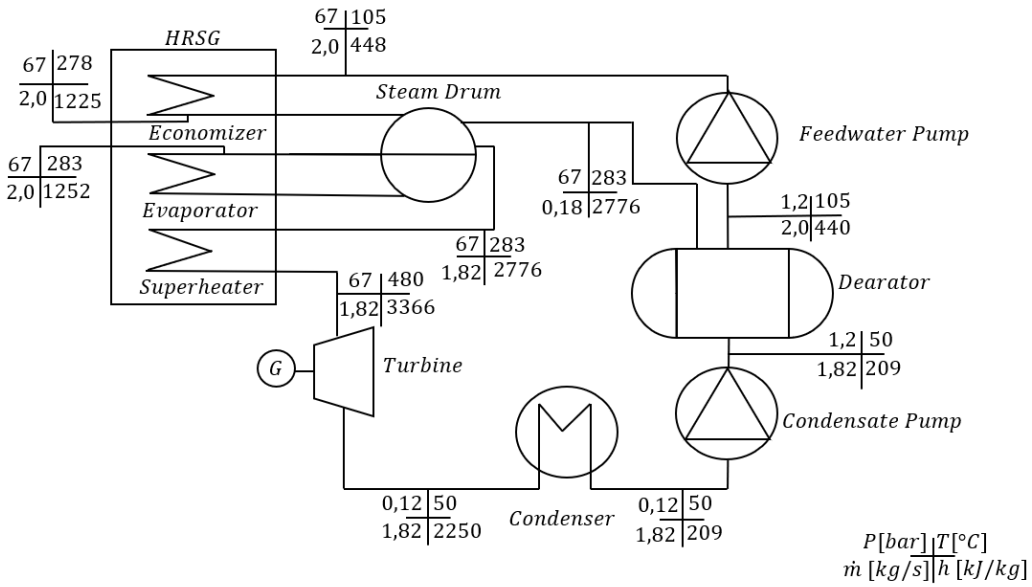

Figure 4.5: SP Rankine cycle with deareator including values shown for pressure, temperature, mass flow and specific enthalpy considered at 67 bar for the HRSG.

The hot and cold fluid mass flow rates and temperatures within the HRSG are used to calculate the heat transfer rates in each heat exchanger section. This includes computing the LMTD applying a specified overall heat transfer coefficients (U), and determining the corresponding heat transfer areas. These values are summarized in Table 4.6.

Section	$T_{hot,in}$ **(°C)**	$T_{hot,out}$ **(°C)**	$T_{cold,in}$ **(°C)**	$T_{cold,out}$ **(°C)**	**LMTD (K)**	Q **(MW)**
Economizer	293	155	105	278	29,3	1,56
Evaporator	563	293	283	283	81,1	3,2
Superheater	650	563	283	480	220,6	1,07

Section	**Overall** U **(W/m^{2}K)**	**Area** $A = Q/(U \cdot \mathbf{LMTD})$ **(m^2)**
Economizer	100	533
Evaporator	50	792
Superheater	50	97

Table 4.6: Temperatures, heat transfer rates and areas for the HRSG involving the economizer, evaporator and superheater with the dearator at a pressure of 67 bar.

In addition to the 67 bar configuration, the SP Rankine cycle operating at 20 bar is also considered. The corresponding cycle values for pressure, temperature, enthalpy, and mass flow rate are presented in Figure 4.6, with detailed results on temperatures, heat duties, and heat exchanger areas provided in Table A.2 in Appendix A.6.

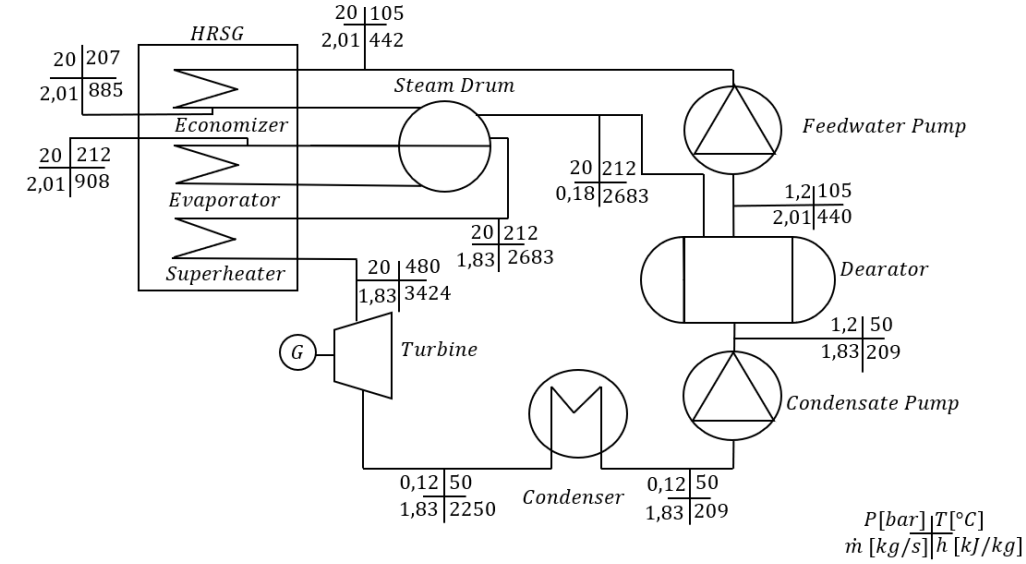

Figure 4.6: SP Rankine cycle with deareator including values shown for pressure, temperature, mass flow and specific enthalpy considered at 20 bar for the HRSG.

Finally, the DP Rankine cycle is analyzed, incorporating the HP stage at 67 bar and a LP stage at 20 bar. The key thermodynamic parameters—pressure, mass flow rate, temperature, and specific enthalpy—for each state point in the cycle are presented in Figure 4.7.

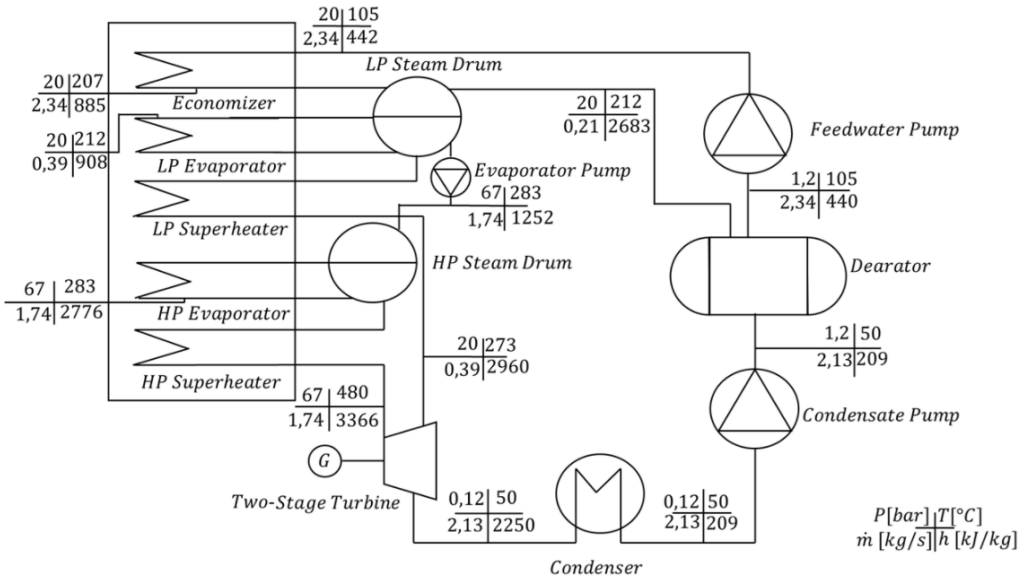

Figure 4.7: DP Rankine cycle with deareator including values shown for pressure, temperature, mass flow and specific enthalpy combined 67 bar and 20 bar as HP and LP respectively.

Analogous to the SP configuration, the heat transfer rates and corresponding heat exchanger areas in the HRSG are computed for the DP case. These results are summarized in Table 4.7.

Section	$T_{hot,in}$ **(°C)**	$T_{hot,out}$ **(°C)**	$T_{cold,in}$ **(°C)**	$T_{cold,out}$ **(°C)**	**LMTD (K)**	Q **(MW)**
LP Economizer	222	130	105	207	19,78	1,03
LP Evaporator	287	222	212	212	33,80	0,744
LP Superheater	293	287	212	273	38,42	0,063
HP Evaporator	566	293	283	283	81,84	3,25
HP Superheater	650	566	283	480	222,07	1,02

Section	**Overall** U **(W/m^{2}K)**	**Area** $A = Q/(U \cdot \textbf{LMTD})$ **(m^2)**
LP Economizer	100	524
LP Evaporator	50	550
LP Superheater	50	32
HP Evaporator	50	995
HP Superheater	50	92

Table 4.7: Temperatures, heat transfer rates and areas for the HRSG involving the economizer, LP and HP evaporator and LP and HP superheater with the dearator evaluated at HP of 67 bar and LP at 20 bar.

A comparison of the performance parameters for the SP and DP Rankine cycles is presented in Table 4.8. This includes thermal efficiency, net power output, heat exchange, and pump work.

Performance Parameters	**SP**	**DP**
η_{RK} $[\%]$	35	36
$\dot{W}_{\text{net}}$ $[MW]$	2,01	2,20
$\dot{W}_{\text{turbine}}$ $[MW]$	2,03	2,22
$\dot{Q}_{\text{cond}}$ $[MW]$	3,71	4,35
$\dot{Q}_{\text{HRSG}}$ $[MW]$	5,73	6,13
$\dot{W}_{\text{cond,pump}}$ $[kW]$	0,2	0,2
$\dot{W}_{\text{fw,pump}}$ $[kW]$	16,2	11,3
$\dot{W}_{\text{evap,pump}}$ $[kW]$	-	5,4

Table 4.8: Summary of performance parameters for the DP and SP Rankine cycles.

As observed by table 4.8 the SP cycle results in a thermal efficiency of 35 %, whereas including the DP configuration leads to a one percentage point increase in the thermal efficiency. This enhancement is accompanied by a slightly higher turbine power output and HRSG heat input. To further examine the thermodynamic behavior of each configuration, the temperature versus heat duty (T–Q) profiles for the HRSG sections are analyzed. These profiles offer insight into heat exchanger performance and the thermal matching between the hot and cold streams. The T–Q diagram for the SP case is first presented in Figure 4.8

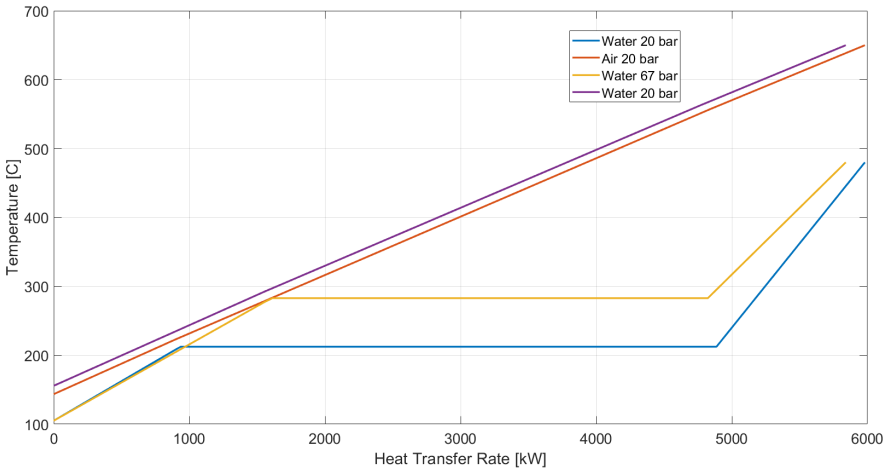

Figure 4.8: Temperature versus heat transfer rate for the SP Rankine cycle at 67 bar and 20 bar. The plot compares temperature profiles at varying pressures within the heat exchanger. It illustrates the thermal interaction and phase change behavior of water during heat absorption, highlighting the effects of pressure on temperature response across the heat exchanger.

Figure 4.8 shows the T–Q diagram of the HRSG in a SP Rankine cycle analyzed at both 20 bar and 67 bar operating pressures. Heat is transferred from hot air to water through sensible and latent heating in the economizer, evaporator, and superheater. Initially, the feedwater is heated through the economizer until it reaches the approach temperature. This heating continues until the water reaches its saturation temperature. In the evaporator, the water undergoes a phase change from liquid to saturated steam which is shown by the horizontal line in Figure 4.8. After the evaporation process, the superheater increases the temperature of the saturated steam to a superheated vapor. The impact of pressure level is evident in Figure 4.8. Increasing the pressure from 20 bar to 67 bar raises the saturation temperature from 212 °C to 286 °C. This increases the mean heat addition temperature and improves thermodynamic efficiency. At 67 bar, the lower latent heat of vaporization results in a shorter evaporation segment and reduced evaporator area. However, at 20 bar, the lower saturation temperature enables greater heat recovery and a lower air outlet temperature, though it requires a larger heat transfer area. The choice between pressure levels reflects a trade-off between efficiency, heat recovery, and equipment size.

Figure 4.9 shows the T–Q diagram for the HRSG in a DP Rankine cycle, combining both 20 bar (LP) and 67 bar (HP) levels.

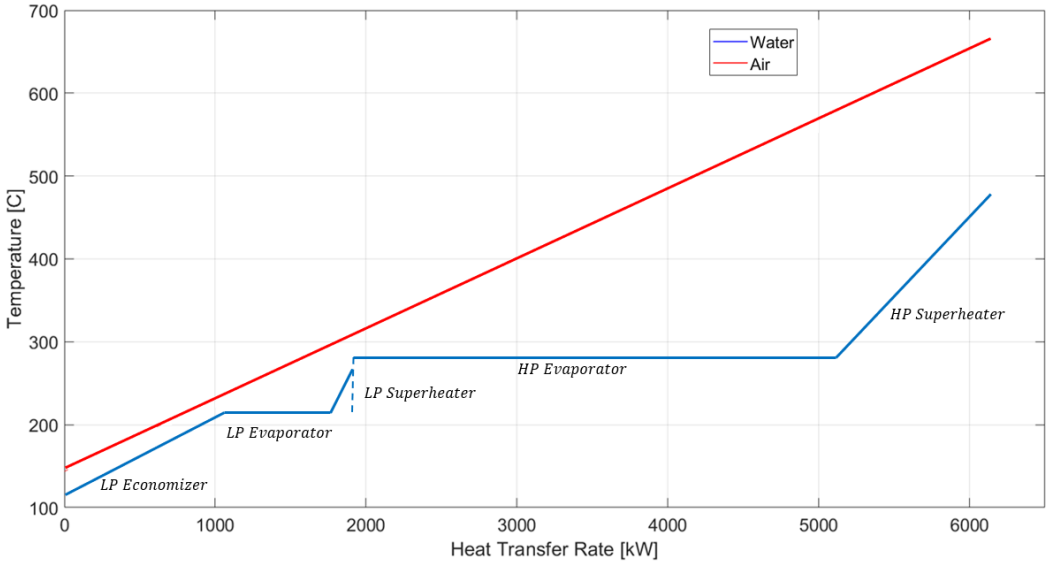

Figure 4.9: Temperature versus heat transfer rate for the DP Rankine Cycle. The plot shows the temperature profiles of air and water across different heat exchanger sections: LP economizer, LP evaporator, LP superheater, HP evaporator, and HP superheater.

Here the red line represents the air temperature profile, while the blue line traces the water temperature changes throughout each heat exchanger in the HRSG for the DP configuration. Similar to a SP configuration, water is initially preheated in the economizer until it reaches the approach temperature. However, the key difference here is the inclusion of two evaporators and two superheaters. The LP evaporator operates at 20 bar, where the temperature remains constant as latent heat is added during the phase change from saturated liquid to saturated vapor. Once evaporation is complete, the LP steam is heated further beyond saturation to 273°C in the LP superheater. A critical transition occurs next: the saturated water must be raised from the LP saturation temperature to the HP saturation temperature. In traditional HRSG designs, this step would occur in a separate HP economizer.

However, in this configuration, no dedicated HP economizer is used. Instead, this enthalpy increase is accounted for within the HP evaporator, and is illustrated by the dashed line in the figure. This dashed segment bridges the thermal gap between the LP and HP saturation temperatures, representing the energy required to increase enthalpy from LP saturated liquid to HP saturated liquid. This alternative approach simplifies the heat exchanger design while still achieving the necessary thermal transition for HP evaporation. Following the dashed transition, another constant-temperature phase occurs, marking the HP evaporator section where saturated water is converted into HP saturated steam. Finally, the HP steam undergoes superheating to approximately 480°C in the HP superheater, ensuring that it carries sufficient thermal energy for expansion. The superheated steam from both the LP and HP stages is then directed to a two-stage turbine, where it drives power generation. The DP configuration enables more effective heat recovery by capturing energy across a broader temperature range. As shown in Figure 4.9, operating a portion of the

cycle at the lower pressure allows additional heat to be extracted from the air, reducing the air outlet temperature. In this case there is a potential for heat recovery when utilizing a lower pressure, which indicates a suitable potential when using the DP Rankine cycle by operating at two different pressure levels, although it should be noted that this comes with a minor decrease in the thermal efficiency. Therefore, this heat recovery potential for the DP Rankine cycle will be examined further through a sensitivity analysis of the cycle, which is presented in Section 5.

Chapter 5

Sensitivity Analysis

The following chapter considers a sensitivity analysis of both the numerical packed bed model and the DP Rankine cycle. The objective of these analyzes is to assess how variations in selected parameters influence system performance.

5.1 Packed Bed Model

A sensitivity analysis is conducted on the packed bed model to evaluate how changes in key parameters affect the temperature distribution and total pressure loss along the bed during operation. The parameters analyzed include:

- Mass flow rate
- Diameter of particles
- Void fraction

Each parameter is varied by $\pm$ 10% relative to a defined reference case, unless otherwise specified. All the parameters will be varied, focusing mainly on the effect for a chosen scenario of 24-hour operation of the charging cycle. The key parameters involved in the numerical packed bed model are listed in Table 4.1 in Section 4.1.

5.1.1 Variation in Mass Flow Rate

The mass flow of air directly affects the heat transfer rate throughout the bed, which thereby influences the temperature distribution. The mass flow is varied by a percentage increase and decrease compared to the reference from Table 4.1. Initially, this temperature distribution is considered for a 24-hour charging cycle, which is shown in Figure 5.1

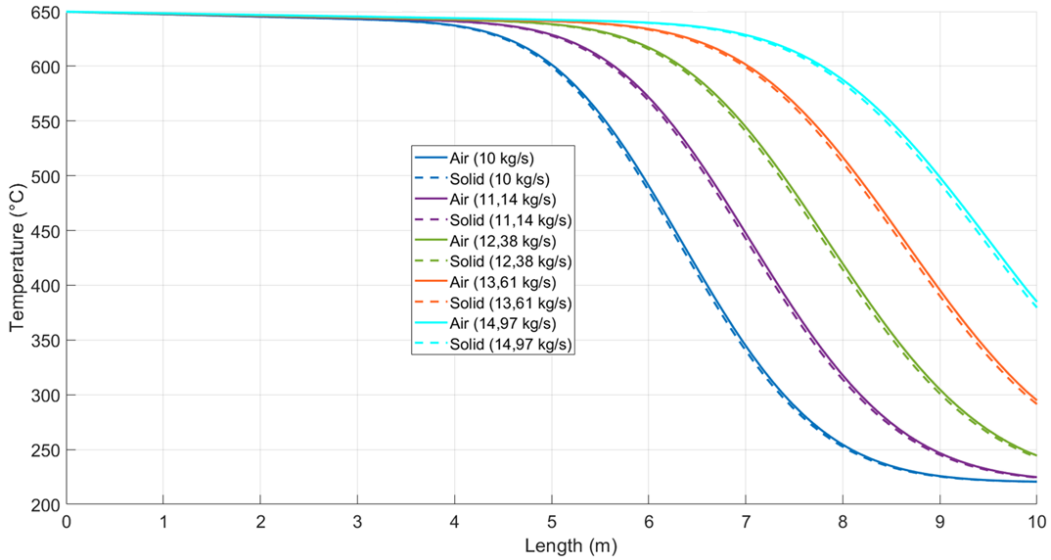

Figure 5.1: Temperature profiles of air and solid media along the packed bed length during the charge cycle, for varying mass flow rates. The graph illustrates the thermal front progression and the effect of increasing air mass flow rate (from 10 to 14.97 kg/s) on heat transfer and temperature distribution within the bed.

Figure 5.1 illustrates the variation in air temperature as a function of the axial length of the numerical model for different mass flow rates during a 24-hour simulation period. The simulation aims to investigate the influence of mass flow rate on the thermal performance and heat transfer characteristics inside the packed bed, which is charged with hot air at approximately 650°C. Hot air is introduced at the inlet and flows in the axial direction through the voids in the packed bed, transferring heat to the solid particles via convective heat transfer. The convective heat transfer is also affected by the convective heat transfer coefficient, whose variation is shown in Figure A.4 in Appendix A.7. Four distinct mass flow rates are simulated: 10.00 kg/s, 12.38 kg/s, 14.50 kg/s, and 18.00 kg/s. The temperature profiles represent the state of the packed bed at the end of the 24-hour charging period. It can be observed that the cyclic charging behavior remains consistent for all mass flow rates, characterized by the formation of a sharp temperature gradient region that advances through the bed and eventually reaches steady-state conditions. Additionally, it can be seen that the temperature increases with a higher mass flow rate of air and decreases with a lower flow rate. This tendency is expected as a higher mass flow increases the heat transfer, leading to a higher temperature along the packed bed. At low air flow rates, the air spends more time in contact with the solid media, resulting in a rapid temperature drop along the bed length. Consequently, the temperature decreases significantly from the inlet, with a steep gradient occurring from approximately 5 m onwards. As the flow rate increases, the temperature profiles shift toward the outlet, indicating less steep gradients and a more uniform high-temperature along the bed. At the highest flow rate examined, the temperature remains high throughout most of the bed length, with a noticeable temperature drop only near the outlet, indicating a nearly fully charged packed bed. As observed, the mass flow rate has a significant impact on the temperature throughout the bed, which will be elaborated further in Section 6.

5.1.2 Variation in Void Fraction

The void fraction affects the density of the packed bed, indicating the proportion of void space within the total volume. This directly influences the flow of fluid through the bed and, consequently, the heat transfer and temperature distribution. A lower value of void fraction implies more contact between the packing elements. Such conditions provide enhancement in heat transfer within the packed bed and hence improvement in the thermal performance of the storage unit. The void fraction is similarly varied by a percentage increase and decrease to observe the impact on the temperature along the bed. It should be noted that the mass of the stones are kept constant in this analysis with varying void fraction, this influence will be discussed upon in Section 6. The void fraction variation is shown in Figure 5.2 for the charging cycle of 24 hours.

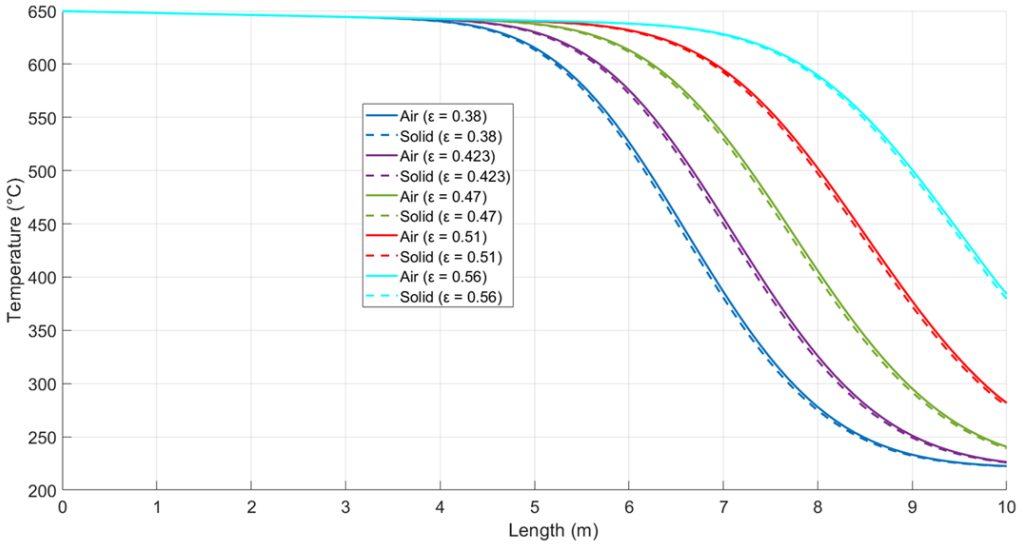

Figure 5.2: Temperature profiles of air and solid media along the packed bed length during the charge cycle, for varying void fraction. The graph illustrates the thermal front progression and the effect of increasing the void fraction on heat transfer and temperature distribution within the bed.

Figure 5.2 presents the axial temperature distribution of the air after 24 hours of charging, for different void fractions ε of the bed. The simulation is considered with a constant air mass flow rate of 12.38 kg/s. As observed, the void fraction influences the thermal interaction between the air and the solid. In this case, the mean temperature increases for a higher void fraction and decreases for a lower fraction. Since less solid material has to be heated up when the void fraction is lower, the temperature will increase compared to a higher void fraction. It can be observed at lower void fraction the temperature is lower along the bed compared to the other void fraction analyzed where the convective heat transfer is lower. As the void fraction increases the heat exchange become more effective consistent with the higher void space and reduced solid-to-fluid contact area. For further increase in the void fraction 0.55 compared to the reference void fraction used according to [von der Heyde, 2022] of 0.47 the temperature is almost uniform along most of the bed, this implies high convective heat transfer as the air passes through the void space, where a higher convective heat is absorbed into the solid material. Besides the temperature variation for the variation in the void fraction it is also influenced by the pressure loss across the bed, which will be further examined in Section 5.1.4.

5.1.3 Variation in Particle Diameter

The effect of varying the diameter of the solid material is considered next. The solid particles are assumed to be spherical. It should be noted that using non-spherical geometry would influence both heat transfer and void fraction, but this is outside the scope of this thesis and is therefore neglected. The variation in diameter also influences the heat transfer and thereby the temperature along the bed. Additionally, the size of the particle will affect the pressure loss through the bed, this will be examined in Section 5.1.4. The variation will be evaluated for the diameter from 15 mm to 50 mm in five intervals. This will be examined for the charging cycle. Figure 5.3, shows the charging cycle for the diameters showing the heat front of the packed bed.

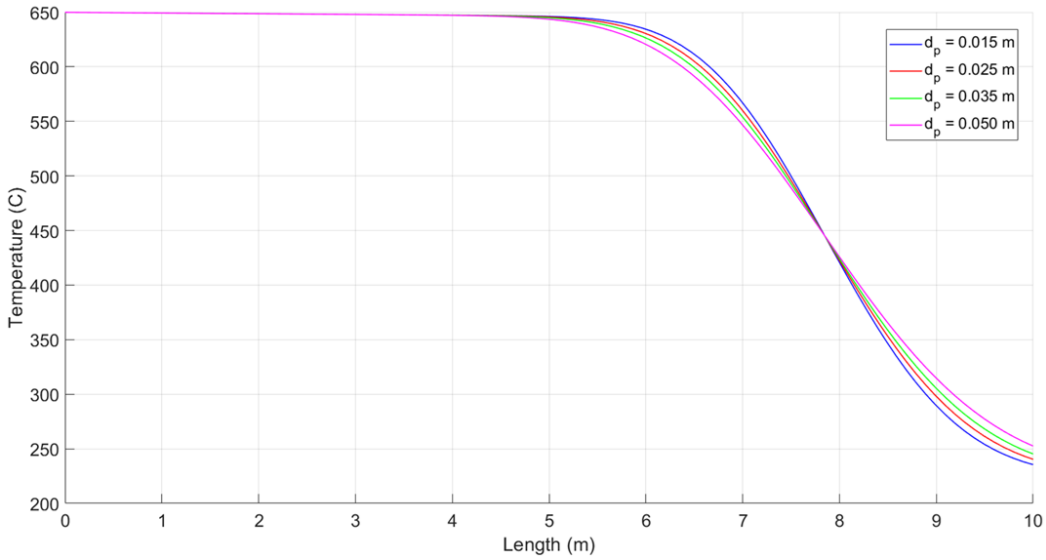

Figure 5.3: Temperature profiles of air along the packed bed length during the charge cycle, for varying particle diameters. The graph illustrates the thermal front progression and the effect of increasing the particle diameter on heat transfer and temperature distribution within the bed.

Figure 5.3 illustrates the effect of particle diameter on the axial air temperature distribution along the bed. The packed bed is assumed to be filled with spherical particles of volcanic rocks as used by [von der Heyde, 2022]. The smallest particle diameter results in the highest mean temperature across the length of the bed. The charging of the packed is improved because the finer particles allow for more efficient heat transfer between the hot air and the solid material. As the particle diameter increases, the temperature gradient becomes less steep, and the thermal front advances less compared to the case with smaller particles. While smaller particle diameters improve thermal performance by enhancing heat transfer, they also lead to higher pressure loss, which will be examined further in the following section.

5.1.4 Pressure Loss

Pressure loss influences both the heat transfer in the bed and the energy consumption of the fan, thereby affecting the overall system performance during charging and discharging. Accurately predicting pressure loss across a packed bed is also essential for estimating the pump power requirements.

This section investigates the pressure loss along the length of the packed bed, focusing on its dependence on mass flow rate, superficial velocity, particle diameter and void fraction. The pressure loss is evaluated by accounting for both the pressure gradient through acceleration and frictional pressure loss. As illustrated in Figure 5.1, the air temperature varies across the bed, leading to changes in air density. To account for this change, the air is assumed to behave as an ideal gas. The pressure loss across the packed bed is evaluated using a reference mass flow rate of 12.38 kg/s, calculated based on the PBTES design from [von der Heyde, 2022], as detailed in Appendix A.4. Figure 5.4 illustrates how the pressure loss varies along the bed for mass flow rates both higher and lower than this reference value.

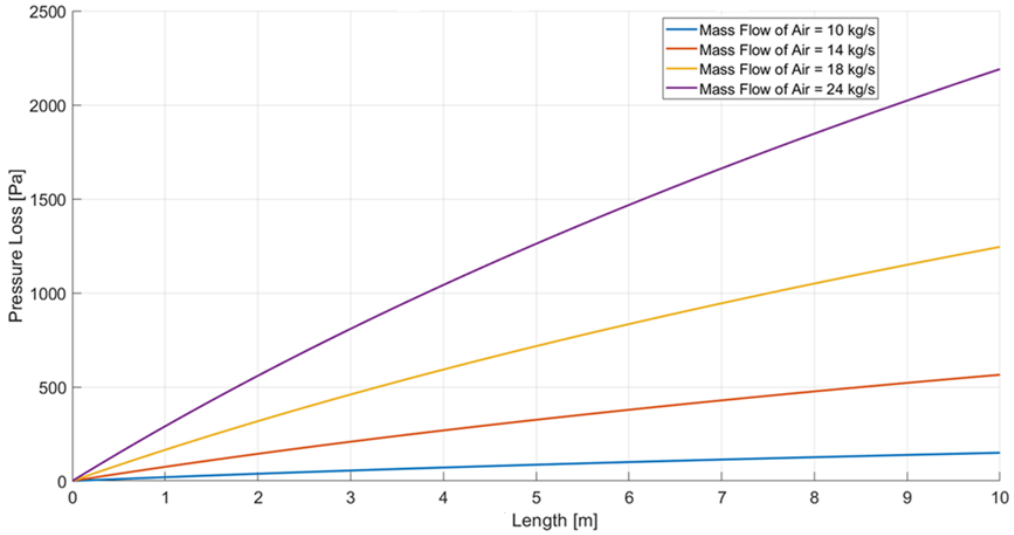

Figure 5.4: Pressure Loss along the packed bed length for varying mass flow rates from 10 kg/s to 24 kg/s.

Figure 5.4 displays four curves representing distinct mass flow rates of air through the bed. It can be observed that the pressure loss increases with bed length for all mass flow rates. This trend is a direct consequence due to friction on the fluid as it navigates through the porous medium. It can also be observed that the pressure loss across bed length shows nonlinear behaviour where the highest pressure loss is for the mass flow rate of air at 24 kg/s. One key factor contributing to the non-ideal behavior in the packed bed is the variation in air density due to temperature fluctuations. Since air density is inversely proportional to temperature, an increase in temperature results in a decrease in density. As a consequence, the pressure gradient varies across the packed bed. The effect of superficial velocity on pressure loss through the packed bed is analyzed next. Superficial velocity, which represents the flow rate per unit cross-sectional area of the bed, is directly linked to the resulting pressure loss. In this analysis, the air velocity is varied from 0 to 2 m/s, following a similar approach as described in [von der Heyde, 2022], to assess its impact on pressure loss. The results are presented in Figure 5.5.

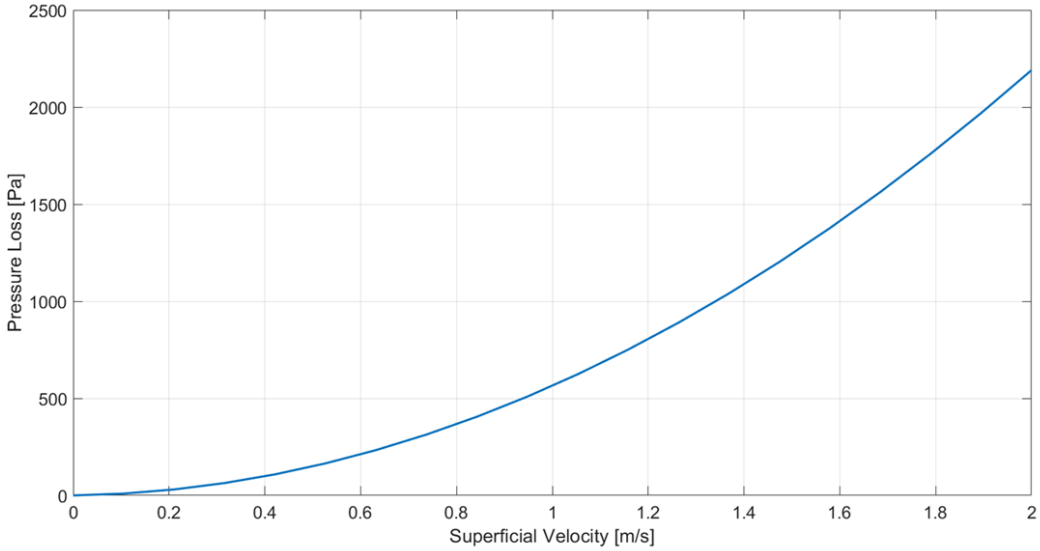

Figure 5.5: Illustration of the pressure loss in relation to the superficial velocity from 0-2 m/s.

The figure shows the variation of pressure loss as a function of the superficial velocity through the packed bed. The curve demonstrates a clear trend in which the pressure loss increases as superficial velocity rises. This behavior is largely governed by the Ergun equation, which accounts for both the viscous and inertial losses in the porous media. At low superficial velocities, the pressure loss is relatively small where viscous effect are dominating through the packed bed. As the superficial velocity increases, the pressure loss rises non-linearly, revealing the increasing influence of inertial forces. This tendency highlights the trade-off between higher flow rates and system efficiency. Careful selection of operating velocity is therefore essential to reduce fan energy consumption and maintain effective heat transfer without incurring excessive pressure losses.

As shown in Figures 5.3 in Section 5, the change in diameter of the particle have minor effects on the temperature distribution along the bed. Since the temperature is higher for a smaller particle diameter, this would seem appropriate for the packed bed and the heat transfer. However, the smaller rock will introduce a higher pressure loss along the bed due to its reduced void fraction and increased surface area per unit volume, which increases resistance to fluid flow and thereby higher frictional losses. This indicates that the size cannot be reduced too much without increasing the pressure loss and thereby the energy requirement for the blower in the overall system. To investigate this, pressure loss is evaluated for particle diameters ranging from 15 mm to 50 mm. The results are shown in Figure 5.6.

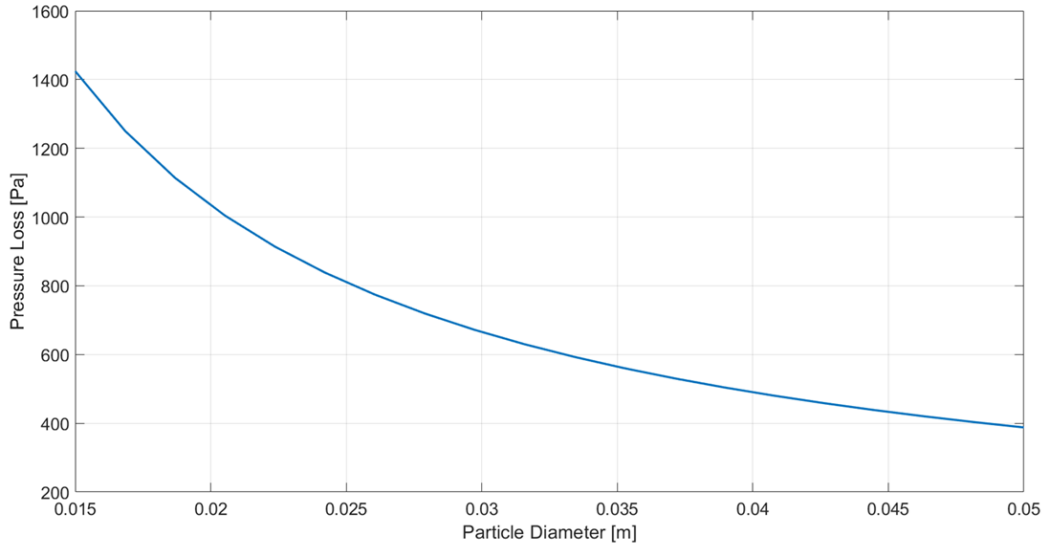

Figure 5.6: Illustration of the pressure loss in relation to the varying particle diameter ranging from 35-50 mm.

Figure 5.6 highlights a key trend: larger particle diameters result in lower pressure losses, whereas smaller particles increase resistance, causing a higher pressure loss. From the Ergun Equation it is evident that particle diameter is inversely proportional to pressure loss. As the particle diameter increases, resistance to fluid flow decreases, leading to a lower pressure loss. Conversely, for small particle diameters, the increased surface area per unit volume results in higher frictional losses and thereby a higher pressure loss. In this case, to obtain a reduced pressure loss during charging and discharging while also taking the effect of the temperature distribution into account, it has been decided to choose a sufficient particle diameter of 35 mm in the packed bed. This is equivalent to the size utilized by [von der Heyde, 2022] of the volcanic rock.

Lastly, the pressure loss for variation in the void fraction has been examined. As mentioned earlier, the void fraction directly influences the flow of fluid through the bed and, consequently, this will also affect the pressure loss for both the charge and discharge cycles. The void fraction is examined through a variation from 0.35 to 0.6. This is shown in Figure 5.7.

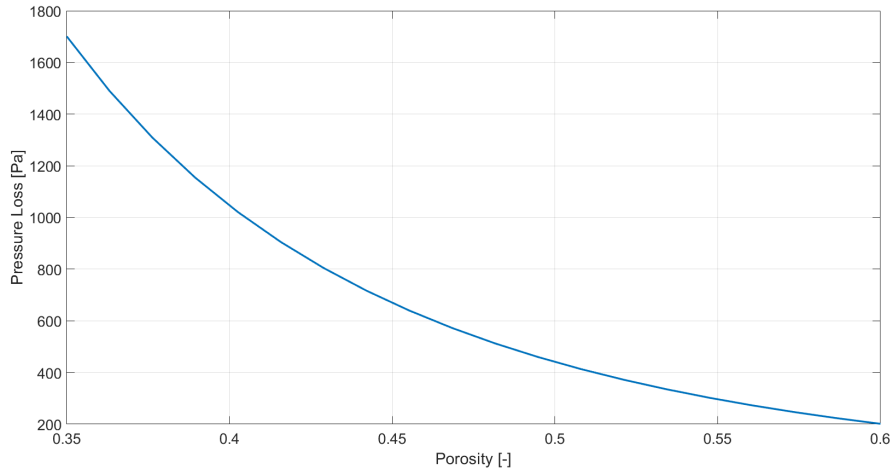

Figure 5.7: Illustration of the pressure loss in relation to the varying void fraction ranging from 0.35 to 0.6.

From Figure 5.7 it can be observed that the variation of pressure loss along bed length for different porosities shows that lower porosity leads to higher pressure losses while higher porosity reduces resistance. The dependency of pressure loss on porosity can be explained by the Ergun Equation, since it has an inverse relationship with pressure loss. Additionally higher porosity decreases pressure loss as the larger void fraction allows fluid to move more freely with less resistance. It should be noted that the mass of the rocks is treated constant in this evaluation for void fraction, this influence will be discussed further in Section 6.

5.2 Sensitivity Analysis of the Dual-Pressure Rankine Cycle Configuration

As mentioned in Section 4.2, there is a potential for heat recovery in the HRSG when operating at different pressure levels. The DP Rankine cycle is examined in this case to investigate the impact of variation in the pressure in the LP evaporator. The LP varies from the initial pressure of 20 bar down to 5 bar. The temperature versus heat transfer rate at the different pressure levels is shown in Figure 5.8. To provide a clearer view of these effects, the dashed line shown in Figure 4.9 in Section 4.2, indicating the enthalpy increase between LP and HP saturation temperatures, is omitted.

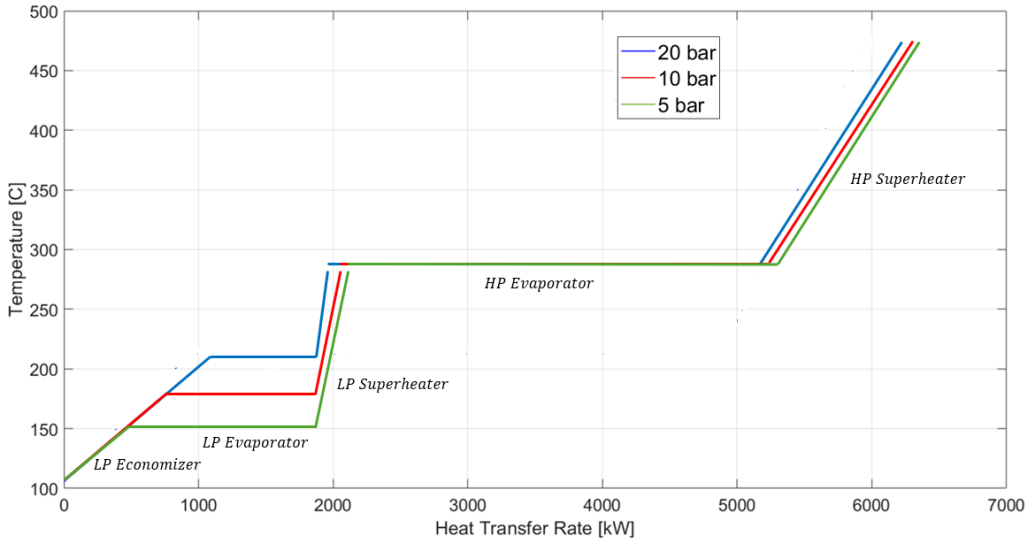

Figure 5.8: Temperature versus heat transfer rate for different LP ranging from 20 to 5 bar in a DP Rankine cycle. The diagram shows the progression of heat transfer through key components: the LP economizer, LP evaporator, LP superheater, HP evaporator, and HP superheater.

Figure 5.8 presents the variation in the water/steam temperature as a function of the heat transfer rate in the HRSG for the DP configuration for different pressure variations in the LP evaporator. Each line in Figure 5.8 corresponds to a different LP evaporator pressure. The economizer raises the temperature of the feedwater to the approach temperature, which is different for each pressure level, as this depends on the specific saturation temperature for the given pressure. Lower LP evaporator pressures reduce the saturation temperature, thereby increasing the heat recovery across the HRSG. However, higher LP evaporator pressures result in elevated saturation temperatures, which can benefit turbine operation but reduce the available thermal gradient for heat extraction. After evaporation, the LP superheater increases the steam temperature to a constant value of 273 °C for all cases. At lower LP pressures, the larger temperature difference between saturation and superheating temperatures leads to a higher heat transfer rate in the superheater. This results in steam conditions more favourable for expansion while further improving heat recovery.

The variation in LP pressure significantly affects the heat transfer characteristics of the LP economizer and LP evaporator. In contrast, the LP superheater and HP evaporator are less sensitive to pressure changes. As LP pressure increases, the required latent heat for evaporation decreases, reducing the heat input needed in the LP evaporator. Additionally, because the steam temperature remains constant at 273 °C, the heat transfer rate in the superheater is relatively unchanged across pressure levels. At 5 bar, the low saturation temperature leads to a greater temperature difference between the air and water, allowing the HRSG to recover more heat. However, at higher LP pressures, this temperature difference narrows, especially in the low-temperature region, leading to lower heat recovery.

The corresponding air temperature profiles are shown in Figure 5.9.

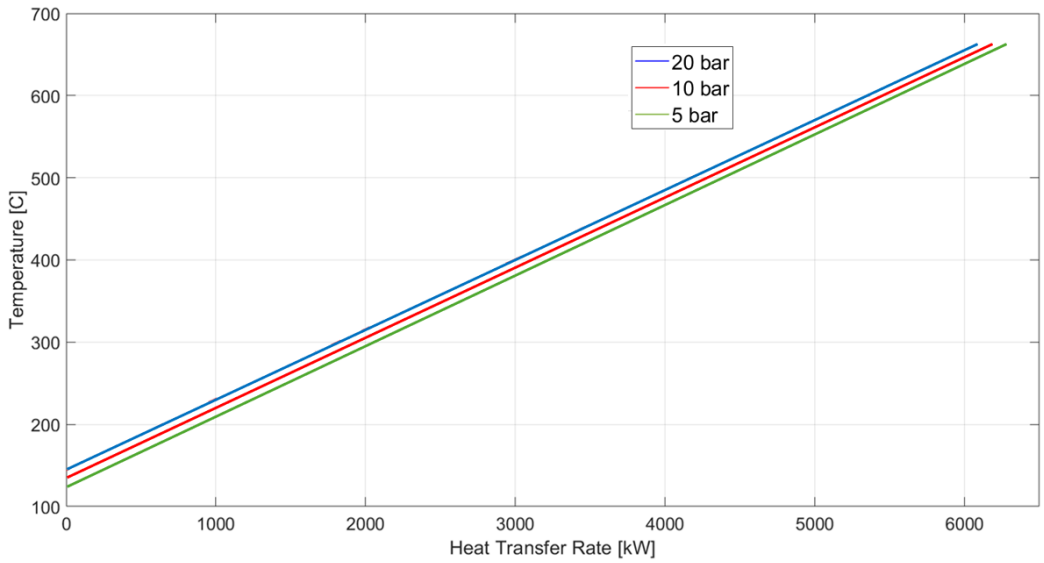

Figure 5.9: Temperature versus heat transfer rate for different LP ranging from 20 to 5 bar in a DP Rankine cycle for the hot air.

In Figure 5.9 the inlet air temperature is held constant at 650 °C. As the air transfers heat to the water/steam across the economizer, evaporator, and superheater, its temperature decreases. At lower LP pressures, the outlet air temperature is lower due to the increased heat recovery, while higher LP pressures result in less heat extracted from the air. Despite improved heat recovery at lower LP pressures, the resulting LP steam has lower enthalpy and temperature. This leads to a slight reduction in thermal efficiency, as shown in Figure 5.10.

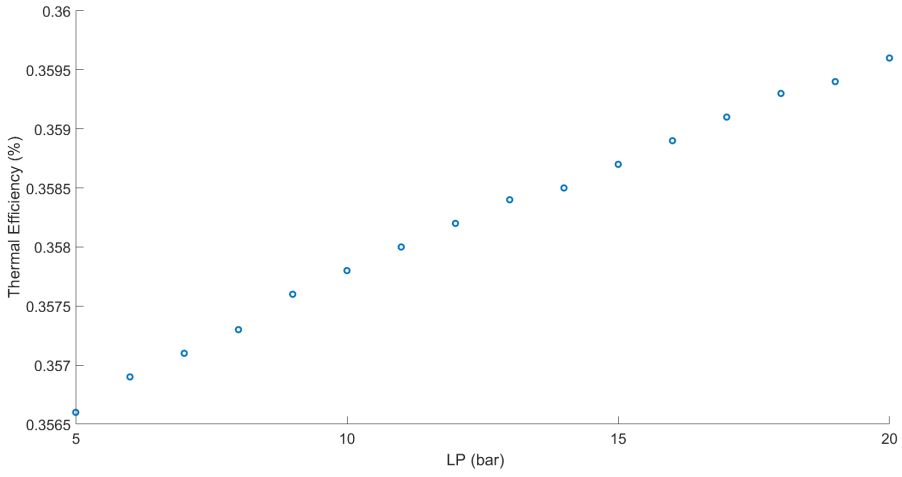

Figure 5.10: Illustration of the thermal efficiency values for variation in the LP ranging from 5 to 20 bar across the HRSG.

Figure 5.10 shows that decreasing the LP evaporator pressure leads to a modest drop in thermal efficiency. This highlights a trade-off: lower pressure increases heat recovery but slightly reduces cycle efficiency. Selecting the optimal LP pressure for the DP Rankine cycle

thus depends on whether heat recovery or cycle efficiency is prioritized. This trade-off is further discussed in Section 6.

5.2.1 Variation in Temperature

This section presents a sensitivity analysis on the impact of inlet air temperature on the thermodynamic performance of the DP Rankine cycle. While the effect of heat losses has been evaluated separately (Section 4.1), these losses are assumed to remain constant with respect to changes in air inlet temperature. They are therefore excluded from this specific analysis. The aim is to isolate the influence of inlet air temperature on cycle performance under idealized operating conditions, assuming constant thermal input from the storage system. It should be noted that round-trip efficiency is not evaluated here due to the varying power-to-heat efficiency across temperature levels. Instead, the analysis focuses on the net power output and thermal efficiency of the Rankine cycle at different inlet air temperatures. The temperature variation of this air inlet significantly impacts the thermodynamic behavior of the cycle, particularly in terms of net work output. This variation is shown in Figure 5.11

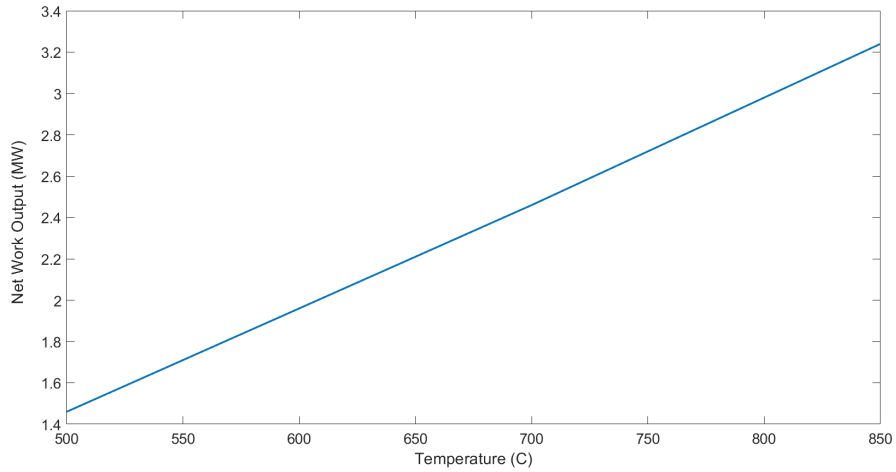

Figure 5.11: Illustration of the net work output of the DP pressure Rankine cycle for variation in the temperature of air inlet to the HRSG ranging from 500 to 850 °C.

As shown in Figure 5.11, the net work output increases consistently with rising air inlet temperature. This is primarily due to the enhanced temperature gradient between the air and the water within the HRSG, which leads to more effective heat transfer. Higher inlet air temperatures allow greater thermal energy absorption in the economizer, evaporator, and superheater sections, resulting in increased steam generation and expansion work in the turbine. The thermal efficiency of a DP Rankine cycle is closely linked to the temperature of the air inlet into the HRSG. Figure 5.12 illustrates the relationship between thermal efficiency and the air inlet temperature in the HRSG.

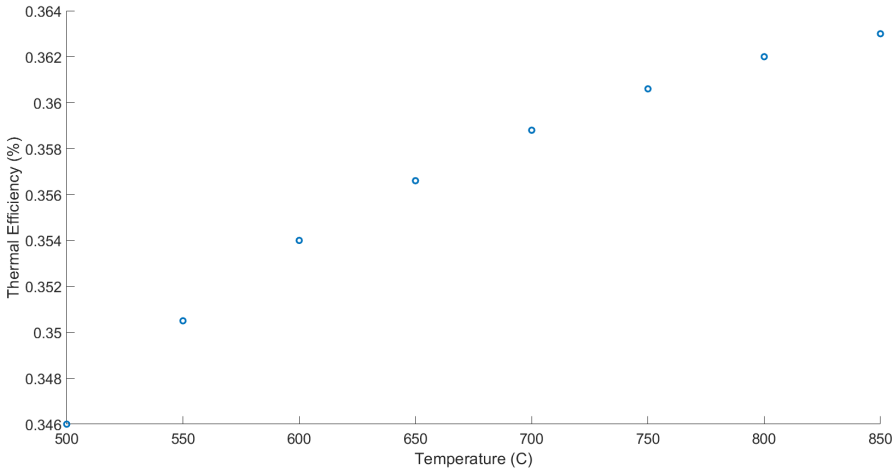

Figure 5.12: Illustration of the thermal efficiency of the DP pressure Rankine cycle for variation in the temperature of air inlet to the HRSG ranging from 500 to 850 °C.

Figure 5.12 indicates that as the air inlet temperature increases, thermal efficiency improves accordingly. At lower air inlet temperatures, the thermal efficiency remains relatively modest. However, as the temperature increases, the efficiency gradually rises, reaching higher values at elevated temperatures. This trend suggests heat recovery from the air inlet can enhance the overall energy conversion process, leading to improved efficiency in the Rankine cycle. In summary, increasing the inlet air temperature enhances both the net work output and the thermal efficiency of the Rankine cycle. Thereby the findings emphasize the potential benefits of utilizing higher temperature from the packed bed in the combined system. However, this improvement in performance must be balanced with material and operational constraints, which will be discussed further in Section 6.

5.3 Summary

A sensitivity analysis was conducted on a PBTES model to evaluate the impact of key parameters on system performance. The study explored the effects of variations in mass flow rate, void fraction, and particle diameter on pressure losses and heat transfer efficiency. Results showed that higher mass flow rates and smaller particle diameters increased pressure loss but enhanced heat transfer. The analysis also included the integration of the storage system with a Rankine cycle, examining how changes in the pressure of the LP evaporator affect the heat recovery potential, whre a decrease in the pressure shows higher heat transfer although this comes with a minor reduction in the thermal efficiency.

Chapter 6

Discussion

The following chapter discusses the integrated system consisting of a Rankine cycle, HRSG, and packed bed TES. It outlines the key modelling assumptions and explains how they influence the accuracy and simplification of the results. Furthermore, the variation of the parameters involved in the sensitivity analysis for the packed bed numerical model and DP Rankine cycle configuration is discussed.

6.1 Viability Analysis

A fundamental aspect of evaluating the viability of the combined system lies in its ability to produce electricity cost-effectively. This is typically assessed through the *Levelised Cost of Electricity* (LCOE), which relates the total costs of building and operating a system to the electricity it produces over its lifetime. According to [von der Heyde, 2022], the reference system consists of a PBTES unit and a simple Rankine cycle integrated with a HRSG, comprising an economizer, evaporator, and superheater. This system also includes a turbine, pump, and condenser. The reference design provides a round-trip efficiency of 25% and a thermal efficiency of 28%.

In this thesis, the Rankine cycle has been extended by adopting a DP configuration and incorporating a deaerator, which improves the thermal integration and energy extraction from the heat recovery process. This modification results in an increased thermal efficiency of approximately 36%. While this efficiency improvement is technically significant, it is necessary to assess whether the gains are economically justified. A higher efficiency system generally incurs additional *Capital Expenses* (CAPEX) due to the cost of added components such as heat exchangers, an extra pump, and the deaerator.

Given that the precise costs of these additional components can vary widely depending on project-specific factors such as size and supplier, this study adopts a simplified economic approach. Specifically, a sensitivity analysis is conducted by incrementally increasing the CAPEX of the DP system while holding all other parameters constant. This approach allows for determining the maximum allowable CAPEX increase that still results in a viable system, defined here as maintaining a lower or equal LCOE compared to the reference system. The economic parameters used for the LCOE calculation are summarized in Table 6.1. These are based on data from [von der Heyde, 2022], with additional assumptions introduced for the improved system.

Economic Parameters	PBTES	DP Rankine Cycle
$LCOE\ [Euro/MWh]$	192	137
$CAPEX/kWh_{el}\ [Euro/MWh]$	100	100
$OPEX/kWh_{el}\ [Euro/MWh]$	40	100
$Lifetime\ [Euro/MWh]$	20	20
$Discount\ Rate\ [\%]$	5	5
$\eta_{h2p}\ [\%]$	28	36

Table 6.1: Economic Parameters for ETES plant by [von der Heyde, 2022] and DP Rankine cycle.

To compute the LCOE, the *Operational Expenses* (OPEX), CAPEX and *Capital Recover Factor* (CRF) is used provided by [von der Heyde, 2022]:

$$LCOE = \frac{\text{CRF} \cdot CAPEX + OPEX}{\eta_{h2p}} \tag{6.1}$$

Where the CFR is given by:

$$\text{CRF} = \frac{r(1+r)^n}{(1+r)^n - 1} \tag{6.2}$$

Where the discount rate is considered to be 5% for 20 operational year which expected amount of time the system by [von der Heyde, 2022] wants to operate. A sensitivity analysis is then performed to evaluate how increases in the CAPEX of the DP Rankine cycle affect its LCOE. The results are shown in Figure 6.1.

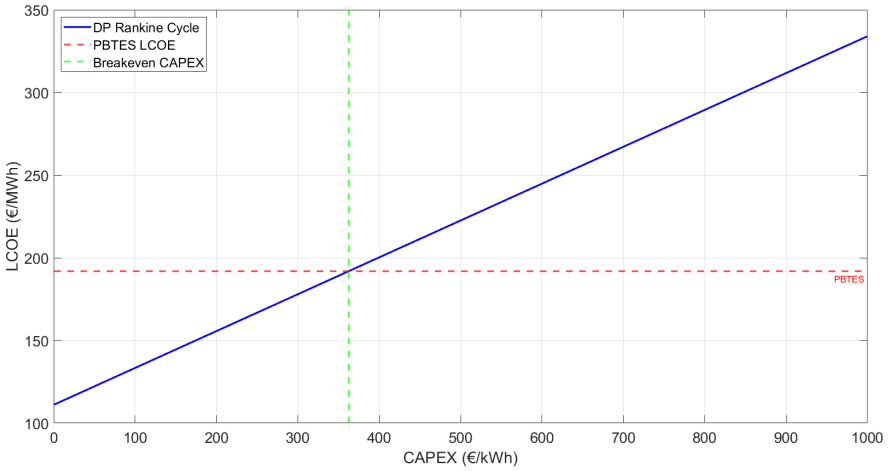

Figure 6.1: Sensitivity analysis showing LCOE as a function of increasing CAPEX for the DP Rankine cycle.

The blue line represents the LCOE of the DP system as CAPEX increases. The horizontal red dashed line indicates the LCOE of the reference PBTES system (192 €/MWh). The vertical green line marks the breakeven CAPEX—approximately 339 €/kWh—beyond which the DP system is no longer economically advantageous. This means that the additional cost of implementing the improved system must not exceed 239 €/kWh beyond the reference CAPEX of 100 €/kWh if the system is to remain cost-competitive. This analysis highlights the crucial trade-off between thermal performance and CAPEX.

Although the efficiency increases from 28% to 36%, the economic feasibility depends strongly on whether this gain can be achieved without exceeding the breakeven CAPEX threshold. Thus, this sensitivity framework establishes a quantitative guideline for decision-makers: if the additional components (deaerator, pump, and extra heat exchangers) can be procured and integrated for less than 239 €/kWh, the upgrade is economically justified under the assumptions made. It should be noted that this analysis assumes constant OPEX and static efficiency over the system's lifetime. It also does not incorporate dynamic electricity prices, degradation effects, or potential downtime, all of which could shift the breakeven point. However, within the scope of this thesis, the analysis provides a valuable preliminary insight into the relationship between technical and economic performance in combined PBTES and Rankine cycle systems.

Another way to optimize the system's performance and economic viability would be most effective to operate the PBTES by charging it during periods of low electricity prices and discharging it during periods of high prices. However, it should be noted that if the PBTES is to be charged when surplus electricity is available and discharged when electricity is needed, in some cases, it means that the TES will not always reach full charge or be fully discharged. Additionally, there will be periods of storage without any charging or discharging activity. Although these storage periods are not considered in this thesis, it is important to note that thermal losses to the surroundings during such idle periods can impact system performance. Over time, these losses can reduce the internal temperature of the TES, which in turn affects the overall efficiency and effectiveness of the PBTES during its operation.

6.2 Assumptions

To simplify the numerical model several assumptions are made. However these assumptions introduce limitations that may affect the accuracy of the results and the interpretation of system performance. One major simplification in the numerical packed bed model is the neglect of radiative heat transfer. This assumption may be reasonable at lower temperatures but becomes less valid since the packed bed reaches temperatures up to 650 °C during operation as shown in Figure 4.1. At these temperatures, radiative heat transfer contributes significantly to the overall heat exchange process. Excluding this mechanism may underestimate heat transfer rates and lead to less accurate predictions of the thermal front progression within the bed. The numerical model also utilizes dry air during the charging and discharging cycle. However including moisture in the air could affect the temperature distribution, as moist air possesses a higher specific heat capacity due to the presence of water vapor. Incorporating humid air properties would enhance the accuracy and realism of the simulation. Additionally the combined system does not consider the modelling of the valves and pipelines. In practical systems, these components influence the overall energy balance, especially since the valves are located before and after the packed bed. Heat losses in piping could lower the air temperature entering the bed, thereby reducing the effective energy available for storage or discharge.

Another significant assumption is neglecting the pressure losses across the heat exchangers within the HRSG. However this can introduce inaccuracies in predicting the overall system performance, affecting steam generation rates, efficiency, and equipment sizing. Pressure loss occurs as the air and water/steam pass through the various heat exchangers mainly due to frictional effects and temperature changes. Additionally the feedwater pump must compensate for pressure losses if included across the HRSG components. These losses could lead to underestimation of pump energy consumption. Additionally the design of the HRSG is not considered however implementing staggered or finned tube arrays could minimize the pressure losses and present a more in depth performance analysis of the HRSG and combined system.

6.3 Sensitivity Analysis and Results

The sensitivity analysis in Section 5 revealed how variation in key parameters influences the thermal performance of the packed bed TES, including the temperature front throughout the bed and the heat recovery potential of the integrated Rankine cycle system. Understanding these dependencies is important to operate the combined system in the most sufficient way.

6.3.1 Packed Bed Thermal Energy Storage

One of the most significant factors affecting the packed bed is the mass flow rate of air. The results in Figure 5.1 revealed that increasing the mass flow rate leads to a higher heat transfer rate thereby maintaining a higher temperature throughout the bed during charging. However, this improvement comes at a cost, as higher flow rates result in greater pressure losses as shown in Figure 5.4 due to increased frictional resistance between the air and solid particles. This, in turn, leads to higher fan energy requirements, which impact the power-to-power efficiency of the combined system. The trade-off between flow rate and efficiency suggests that an optimal mass flow rate of air should be determined based on the system's operation constraints.

Additionally, changes in void fraction reduced the flow resistance but decreased thermal contact between the air and the solid media, leading to broader thermal fronts and reduced discharge temperatures. Thus, a moderate void fraction according to Figures 5.7 and 5.2 (around 0.45–0.5) appears to offer a suitable compromise between thermal performance and pressure loss. It should be noted that the mass of solid inside the bed is kept constant during this analysis. However by keeping this constant, the volume of the solid will also be fixed, which implies that if the void fraction is increased, the total volume of the bed will also increase and if the void fraction is decreased, the volume of the bed will be decreased. For a physical packed bed the volume is usually fixed, so in this case the variation in the void fraction may not always be accurate because the solid mass would vary unless the shape of the solids are changed.

Similarly, particle diameter affects both heat transfer and pressure loss. Smaller particles improve convective heat transfer due to a higher surface area-to-volume ratio, leading to sharper thermal fronts and improved energy recovery. However, they also increase pressure loss, raising fan power requirements. Based on the results, a particle diameter around

35 mm appears to offer a suitable compromise between thermal effectiveness and pressure loss, supporting efficient operation in both charging and discharging modes. The air temperature, particularly during discharge, also influences system performance. Higher air temperatures improve heat recovery and increase power output from the Rankine cycle and HRSG. However, this must be balanced against material limitations and higher energy input requirements. Elevated temperatures increase demands on the electric heater, fan, and pump, potentially raising operational costs. Therefore, while higher temperatures improve thermal performance, they also necessitate a careful evaluation of material durability and system economics.

6.3.2 Rankine Cycle

This thesis evaluated the effect of varying the LP in the DP Rankine cycle. The results indicate that lower LP improve heat recovery from the discharged air by enabling more thermal energy extraction. However, this benefit comes at the expense of slightly lower thermal efficiency in the Rankine cycle due to reduced steam enthalpy. The results in Figure 5.8 indicate a trade-off where a mid-range LP pressure provides a suitable balance between increasing the heat recovery and maintaining overall Rankine cycle efficiency. In this analysis, the approach temperature and pinch point temperature difference were held constant. These parameters significantly influence heat exchanger sizing, steam generation, and overall heat recovery performance. The pinch point temperature difference defined as the smallest temperature difference between the hot air stream and the water in the evaporator limits the extent of heat transfer. Reducing the pinch point in the LP evaporator could enhance the recovery of low-grade heat from the air stream, albeit at the cost of increased heat exchanger surface area.

Similarly, the approach temperature difference, defined as the temperature difference between the steam saturation temperature and the outlet temperature of the economizer, affects how effectively feedwater is preheated before entering the evaporator. A lower approach temperature difference can improve preheating, which in turn increases thermal efficiency and total heat recovery. However, if the approach temperature is too low, the feedwater enters the evaporator near saturation conditions, significantly increasing the required heat transfer area. Finally, integrating a DP Rankine cycle with multistage turbines presents a potential strategy for further improving thermal efficiency. Multistage turbines facilitate steam expansion across multiple pressure levels, optimizing energy extraction.

Overall, the sensitivity analysis confirms that when operating the packed bed and integrated system, careful balancing of thermal performance, pressure loss, and energy input is required. Parameters such as air flow rate, void fraction, particle size, and operating temperature must be tuned to achieve the desired efficiency without compromising system reliability or cost-effectiveness.

Chapter 7

Conclusion

This thesis investigated the performance of a packed bed thermal energy storage (PBTES) system integrated with a Rankine cycle. The study focused on modelling the system using a one-dimensional, transient numerical approach to simulate temperature distribution and heat transfer during charge and discharge cycles. A sensitivity analysis was performed to assess the influence of key parameters, including particle diameter, mass flow rate, and void fraction, on system behaviour. Additionally, the integration of a *Dual-Pressure* (DP) Rankine cycle during discharge was analyzed to determine its impact on heat-to-power efficiency.

A one-dimensional, transient numerical model was developed to simulate the temperature evaluation and heat transfer involved in the PBTES system during charging and discharging cycles. The numerical model of the PBTES was based on governing equations for energy conservation in both solid and fluid phases who were discretized using explicit finite-difference methods. The numerical model captured the transient behavior of the packed bed, demonstrating a temperature evolution and heat transfer during charge and discharge operations across the packed bed. A verification of the numerical model against reference data from the PBTES demonstration plant in Hamburg was considered, showing close agreement, confirming the reliability of the numerical model in predicting system behavior.

The sensitivity analysis revealed that changes in particle size, mass flow rate, and void fraction have significant effects on heat transfer and pressure loss within the packed bed. A higher mass flow rate increased convective heat transfer, accelerating thermal charging while also leading to greater pressure losses. Variations in void fraction influenced both thermal efficiency and pressure loss, where a moderate void fraction around a value of 0.45-0.5 provided a suitable balance between effective heat transfer and manageable airflow resistance. Additionally, reducing particle diameter enhanced heat transfer rates due to increased contact surface area, but also resulted in elevated pressure losses, indicating a trade-off between thermal performance and energy consumption by the fan.

Integrating a DP Rankine cycle demonstrated potential advantages in improving heat recovery from the HRSG while maintaining a thermal efficiency of approximately 36%, compared to 35% for the SP cycle. Lower LP evaporator pressures enhanced heat recovery and reduced air outlet temperatures, but this also led to a slight reduction in the thermal efficiency. A sensitivity analysis of LP evaporator pressures ranging from 5 to 20 bar revealed that while heat recovery increased at lower pressures, thermal efficiency decreased marginally. The study also indicated that increasing the temperature of the air entering the HRSG contributed to higher net electricity generation. For example, an inlet air temperature of 650°C resulted in a net work output of around 2 MW.

From an economic perspective, the feasibility of the PBTES system was assessed using Levelized Cost of Electricity. While improvements in thermal efficiency were achieved with the integration of a deaerator and a DP Rankine cycle, *capital expenditures* (CAPEX) needed to remain below a breakeven threshold to ensure cost-effectiveness. The analysis indicated that the system would remain economically viable as long as additional CAPEX did not exceed 239 $/kWh$ beyond the baseline cost of 100 $/kWh$. These findings emphasize the necessity of balancing cost and performance in system design. Future research should explore dynamic electricity pricing scenarios to determine optimal operational strategies and further refine economic assessments.

In summary, this thesis demonstrates that a one-dimensional, transient numerical model can effectively simulate the thermal behavior of a PBTES system and quantify its interaction with a Rankine cycle. Key operational parameters such as particle diameter, mass flow rate, and void fraction significantly influence thermal and hydraulic performance, requiring careful trade-off analysis. Moreover, integrating a DP Rankine cycle offers a meaningful efficiency improvement, enhancing the viability of ETES systems as a flexible, renewable-aligned storage technology.

Chapter 8

Future Work

The following chapter explores opportunities and topics relevant to further investigation. This includes improving the packed bed model and the combined Rankine cycle through a dynamic model. It also examines the inclusion of an economic and feasibility analysis of the combined system.

8.1 Numerical Packed Bed Model

The current numerical model is developed as a transient, one-dimensional, two-phase approach to simulate the charging and discharging of the packed bed. Future work could significantly benefit from developing a more detailed three-dimensional, dynamic model to better capture spatial temperature variations and non-uniformities within the bed. Furthermore, incorporating variable operational conditions, such as dynamic or load-following scenarios, into the Rankine cycle model would enable more realistic simulations that reflect the fluctuations in electricity supply and demand.

The current model neglects wall effects, which can lead to significant temperature gradients near the boundary. Including these effects would enhance the model's accuracy. Additionally, the model assumes a low Biot number for the solid particles, implying uniform internal temperature. However, the impact of the Biot number has not been examined in depth. A deeper investigation into the influence of the Biot number could provide a more realistic description of internal heat conduction within the particles. While this thesis uses volcanic rock based on a system implemented in Germany, exploring alternative storage media could identify materials with better thermal properties or lower costs. Furthermore, since the geometry of the packed bed is fixed in this thesis, future work could focus on optimizing its dimensions, such as length, diameter, and height to achieve maximum ES efficiency at the lowest cost.

8.2 Economical and Feasibility Analysis

This thesis includes only a basic LCOE analysis for the combined system. A more comprehensive economic assessment should be conducted to evaluate the full feasibility of implementing such systems on a commercial scale. The natural continuation of this thesis will be to obtain the installation cost and the breakeven point for an investment in the combined system of the packed and Rankine cycle. The economic analysis could include different operations, including a sensitivity analysis in relation to the variation in electricity price to determine if the investment in the system is going to be worthwhile over a lifetime period. Additionally, it could be relevant to include an analysis of the demand for electricity to determine realistic discharge periods for the system and investigate when the system is most appropriate for operation.

8.3 Packed Bed Model and Rankine Cycle

The choice of working fluid has a significant impact on system performance. While this thesis uses air as the heat transfer medium, future research could explore alternatives such as molten salt or water, which offer superior thermophysical properties. These fluids may enable higher storage densities and reduce spatial requirements, leading to cost savings. Furthermore, in the current configuration, the Rankine cycle uses water as the working fluid. Future research could explore replacing this with an organic fluid, particularly in applications where lower-temperature heat recovery is desired. Organic Rankine cycles (ORCs) often offer better efficiency under such conditions and could present a viable alternative to the traditional Rankine cycle setup. Another area worth developing is the inclusion of piping and valve dynamics in the model. Although neglected in this thesis, these components influence the thermal losses and overall performance of both the packed bed and Rankine cycle. Modelling them would contribute to a more accurate and realistic representation of the complete system.

Bibliography

[Allen et al., 2013] Allen, K., von Backström, T., and Kröger, D. (2013). Packed bed pressure drop dependence on particle shape, size distribution, packing arrangement and roughness. *Powder Technology*, 246:590–600.

[Anderson et al., 2015] Anderson, R., Bates, L., Johnson, E., and Morris, J. F. (2015). Packed bed thermal energy storage: A simplified experimentally validated model. *Journal of Energy Storage*, 4:14–23.

[Cengel et al., 2017] Cengel, Y. A., Cimbala, J. M., and Turner, R. H. (2017). *Fundamentals of Thermal-Fluid Sciences*. McGraw-Hill Education, 5 edition.

[Dumont et al., 2020] Dumont, O., Frate, G. F., Pillai, A., Lecompte, S., De paepe, M., and Lemort, V. (2020). Carnot battery technology: A state-of-the-art review. *Journal of Energy Storage*, 32:101756.

[Eggers et al., 2022] Eggers, J. R., von der Heyde, M., Thaele, S. H., Niemeyer, H., and Borowitz, T. (2022). Design and performance of a long duration electric thermal energy storage demonstration plant at megawatt-scale. *Journal of Energy Storage*, 55:105780.

[Eller and Gauntlett, 2017] Eller, A. and Gauntlett, D. (2017). Energy storage trends and opportunities in emerging markets. Technical report, International Finance Corporation (IFC) and Energy Sector Management Assistance Program (ESMAP).

[Elsevier, nd] Elsevier (n.d.). Energy storage. Accessed May 4, 2025.

[International, 2025] International, E. (2025). Power prices and estimated power production.

[IPPC, 2021] IPPC (2021). Climate change widespread, rapid, and intensifying – ipcc.

[Khan et al., 2022] Khan, M. I., Asfand, F., and Al-Ghamdi, S. G. (2022). Progress in research and technological advancements of thermal energy storage systems for concentrated solar power. *Journal of Energy Storage*, 55:105860.

[Koefoed, 2013] Koefoed, J. (2013). Thermal exergy and its storage. In KOVACH, E. G., editor, *Thermal Energy Storage*, pages 5–10. Pergamon.

[Mao, 2016] Mao, Q. (2016). Recent developments in geometrical configurations of thermal energy storage for concentrating solar power plant. *Renewable and Sustainable Energy Reviews*, 59:320–327.

[Marongiu et al., 2019] Marongiu, F., Soprani, S., and Engelbrecht, K. (2019). Modeling of high temperature thermal energy storage in rock beds – experimental comparison and parametric study. *Applied Thermal Engineering*, 163:114355.

[Mostafa et al., 2020] Mostafa, M. H., Abdel Aleem, S. H., Ali, S. G., Ali, Z. M., and Abdelaziz, A. Y. (2020). Techno-economic assessment of energy storage systems using annualized life cycle cost of storage (lccos) and levelized cost of energy (lcoe) metrics. *Journal of Energy Storage*, 29:101345.

[Muhammad, 2022] Muhammad, Y. (2022). *Decarbonization of industrial sector through rock based high-temperature thermal energy storage: Experimental, numerical and techno-economic analysis*. PhD thesis.

[Paraschiv and Paraschiv, 2023] Paraschiv, L. S. and Paraschiv, S. (2023). Contribution of renewable energy (hydro, wind, solar and biomass) to decarbonization and transformation of the electricity generation sector for sustainable development. *Energy Reports*, 9:535–544. Technologies and Materials for Renewable Energy, Environment and Sustainability.

[Rabi' et al., 2024] Rabi', A. M., Radulovic, J., and Buick, J. M. (2024). Packed bed thermal energy storage system: Parametric study. *Thermo*, 4(3):295–314.

[Schumann, 1929] Schumann, T. (1929). Heat transfer: A liquid flowing through a porous prism. *Journal of the Franklin Institute*, 208(3):405–416.

[Springer, 2006] Springer (2006). *VDI Heat Atlas*. Springer.

[Versteeg and Malalasekera, 2007] Versteeg, H. K. and Malalasekera, W. (2007). *An Introduction to Computational Fluid Dynamics: The Finite Volume Method*. Pearson Education, 2 edition.

[von der Heyde, 2022] von der Heyde, M. (2022). Electric thermal energy storage based on packed beds for renewable energy integration.

[Wahab et al., 2023] Wahab, H. A., Abdulkareem, A. S., and Abdulrahman, S. A. (2023). Design of rankine cycle using matlab software. *Energy and Power Engineering*, 15(11):277–285.

[Zanganeh et al., 2012] Zanganeh, G., Pedretti, A., Zavattoni, S., Barbato, M., and Steinfeld, A. (2012). Packed-bed thermal storage for concentrated solar power – pilot-scale demonstration and industrial-scale design. *Solar Energy*, 86(10):3084–3098.

Appendix A

Appendix

A.1 Biot Number

The Biot number is a dimensionless parameter used to assess the internal temperature distribution within a solid particle. It compares the internal conductive resistance to the external convective resistance. When Bi < 0.1, it is generally assumed that the temperature inside the particle is spatially uniform, allowing a lumped thermal model to be used. The Biot number is calculated using the following relation:

$$Bi = \frac{h \cdot d_p}{k_s} \tag{A.1}$$

Where h is the convective heat transfer coefficient, d_p is the particle diameter, and k_s is the thermal conductivity of the solid material. Air properties and flow conditions are used to determine the velocity, Reynolds number, Nusselt number and thereby the Biot number for the particle. The calculated Biot number for the varying particle diameter between 0.01 m and 0.06 m is shown in Figure A.1

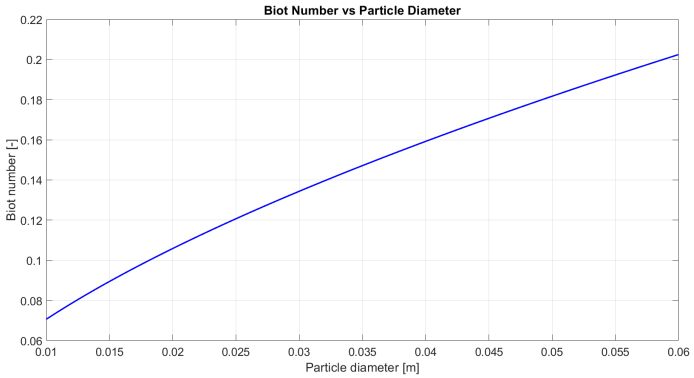

Figure A.1: Calculated Biot Number for the solid particles in the packed bed with variation in the particle diameter from 10 mm to 60 mm.

Figure A.1 shows that for low particle diameters below 35 mm, the Biot number remains below 0.1, supporting the assumption of uniform internal temperature. As the diameter increases, the Biot number becomes higher, suggesting that a lumped model assumption may no longer be appropriate, and internal conduction modelling may be required for accurate heat transfer calculations. However, this increasing impact on the heat transfer throughout the bed is neglected.

A.2 Boundary and Initial Conditions

The boundary and initial conditions are defined for the solid material and the air as shown in Table A.1

	Charge	**Storage**	**Discharge**
Initial condition	$T_{\text{air}}(j=0) = T_{\text{amb}}$	$T_{\text{air}}(j=0) = T_{\text{in}}$	$T_{\text{air}}(j=0) = T_{\text{in}}$
	$T_{\text{stone}}(j=0) = T_{\text{amb}}$	$T_{\text{stone}}(j=0) = T_{\text{in}}$	$T_{\text{stone}}(j=0) = T_{\text{in}}$
Boundary condition	$T_{\text{air}}(i=0) = T_{\text{in}}$	$\frac{\partial T_{\text{air}}}{\partial L} = 0$	$T_{\text{air}}(i=0) = T_{\text{amb}}$
	$\frac{\partial T_{\text{air}}}{\partial L} = 0$	$\frac{\partial T_{\text{air}}}{\partial L} = 0$	$\frac{\partial T_{\text{air}}}{\partial L} = 0$
	$\frac{\partial T_{\text{stone}}}{\partial L} = 0$	$\frac{\partial T_{\text{stone}}}{\partial L} = 0$	$\frac{\partial T_{\text{stone}}}{\partial L} = 0$

Table A.1: Initial and boundary conditions for charge, storage, and discharge phases.

Here, i indicates the spatial direction, j represents the temporal direction, and L is at the end of the packed bed. During charging, the initial temperatures of both the air and the solid are set to ambient conditions. The air enters the system at a fixed temperature, while the outlet is treated as a fixed temperature gradient set to zero. For the solid, fixed temperature gradients are set to zero at both the inlet and outlet of the bed. During storage, no airflow occurs throughout the bed, and the initial conditions for both air and solid are based on a fixed temperature. The boundary conditions for the solid and air are also treated as fixed temperature gradients. During discharge, the conditions are similar to those in charge, with the primary difference being the temperature levels involved.

A.3 Area of Heat Recovery Steam Generator Versus Pinch Point Temperature Difference

The area is examined in relation to the variation in the pinch point temperature difference. This is shown in Figure A.2

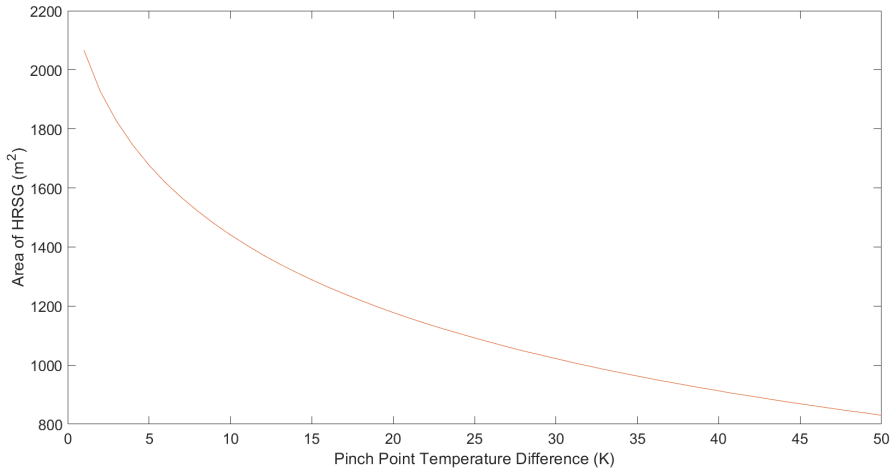

Figure A.2: Area of HRSG versus variation in pinch point temperature difference.

Figure A.2 illustrates the relationship between pinch point temperature difference and the HRSG area. The x-axis represents the pinch point temperature difference, ranging from 0 to 50 K, while the y-axis represents the corresponding heat transfer area required for the HRSG, spanning from approximately 800 to 2200 m^2. In this case, the tendency indicates an increasing area as the pinch point temperature difference approaches zero leading to a higher heat recovery in the HRSG. While this design approach improves the heat recovery efficiency, it results in increased material costs and larger equipment sizes.

A.4 Energy Stored in the Packed Bed

The initial energy stored in the packed bed contains the rocks and the air. The energy stored in the rocks is calculated using the mass of the rocks, specific heat capacity and temperature difference approaching the charging temperature of 650 °C according to [von der Heyde, 2022]. The energy in the rocks are calculated using Equation A.2

$$E_{stored} = m_{stone} \cdot c_{p,S} \cdot (T_{final} - T_{initial}) \tag{A.2}$$

This is found to be 130 MWh, which is equivalent to the energy stored according to [von der Heyde, 2022]. The energy stored in the packed bed by the air is considered next. This uses the same temperature difference, the specific heat capacity of air. The energy stored in the air is calculated by Equation A.3

$$E_{air} = \varepsilon \cdot \rho_{air} \cdot V_{bed} \cdot c_{p,air} \cdot (T_{final} - T_{initial}) \tag{A.3}$$

The energy of air stored is found to be 0,025 MWh. This represents 0,01% compared to the 130 MWh stored in the air and is therefore neglected in the analysis of the packed bed. The mass of air is found using Equation A.5

$$m_{air} = \varepsilon \cdot \rho_{air} \cdot V_{bed} \tag{A.4}$$

This is found to be 230 kg, which is 0,02% of the 1000 ton occupied by the stones and is therefore not taken into account in the analysis of the packed bed.

Additionally, the mass flow rate estimated and used for the numerical model during charging and discharging is found using the superficial velocity provided by [von der Heyde, 2022] to be 0.25 m/s. The density of air is assumed to be found at the initial temperature of 224 °C and looked up at 1 atm. This density is found to be 0.7 kg/m^3. The mas flow of air through the bed are thereby determined using Equation A.5

$$\dot{m}_{air} = \rho_{air} \cdot V_{air} \cdot A_{bed} \tag{A.5}$$

This mass flow is found to be 12.38 kg/s. This is used through the verification of the numerical model compared to the PBTES by [von der Heyde, 2022].

A.5 Grid Indepence Study

A grid independence study is conducted for the packed bed model to ensure that the numerical results are not significantly influenced by the discretization of the domain and to confirm that the model has reached convergence. The simulation is performed for the charging cycle over a 24 hour period, with the inlet air temperature at 650 ° C. The mass flow rate is set to 12.38 kg/s. Figure A.3 shows the temperature distribution along the length of the bed for discretizations using 50, 100, 200, and 400 cells.

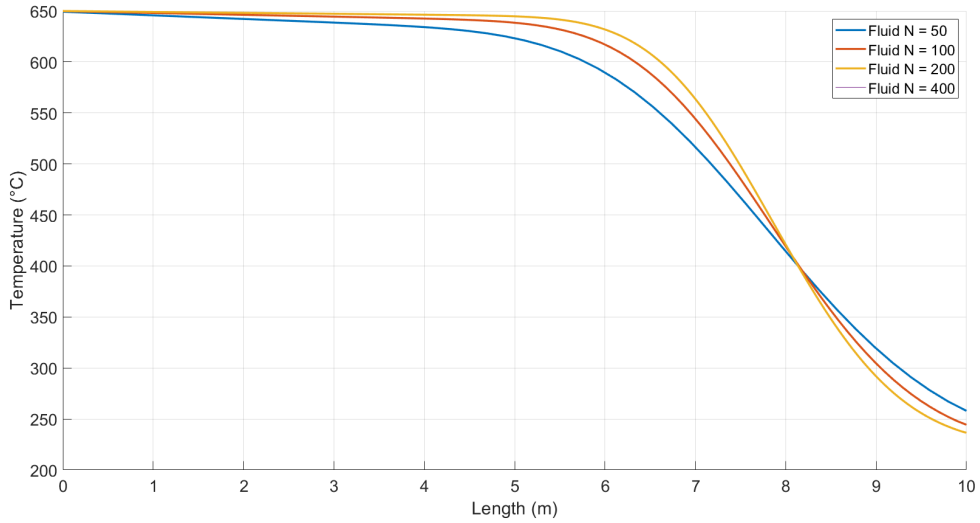

Figure A.3: Variation in cells for the temperature distribution across the bed.

As shown in the figure, increasing the number of grid cells results in only minor changes in the temperature profile during the discharging process. The difference in results between the 200- and 400-cell cases is negligible, indicating that 200 cells are sufficient to achieve grid-independent results while also reducing computational cost.

A.6 Single Pressure Rankine cycle

The mass flow rates and the temperatures involved in the hot and cold fluid in the HRSG are used to determine the heat transfer rates, which include the LMTD values and defined

U values for the three heat exchangers, thereby the heat transfer area can be found. These corresponding values are presented in Table A.2 for the 20 bar configuration.

Section	$T_{hot,in}$ **(°C)**	$T_{hot,out}$ **(°C)**	$T_{cold,in}$ **(°C)**	$T_{cold,out}$ **(°C)**	**LMTD (K)**	Q **(MW)**
Economizer	222	143	105	207	24,95	0,891
Evaporator	557	222	212	212	94,59	3,95
Superheater	650	557	212	480	247,23	1,14

Section	**Overall** U **(W/m^{2}K)**	**Area** $A = Q/(U \cdot \textbf{LMTD})$ **(m^2)**
Economizer	100	357
Evaporator	50	835
Superheater	50	92

Table A.2: Temperatures, heat transfer rates and areas for the HRSG involving the economizer, evaporator and superheater with the dearator at a pressure of 20 bar.

A.7 Variation in Convective Heat Transfer Coefficient

The convective heat transfer coefficient h represents the rate at which heat is exchanged between the air and the stones within the packed bed. This coefficient also affects the temperature gradient along the length of the bed. Figure A.4 illustrates how varying h affects the temperature distribution along the bed length during the discharging cycle.

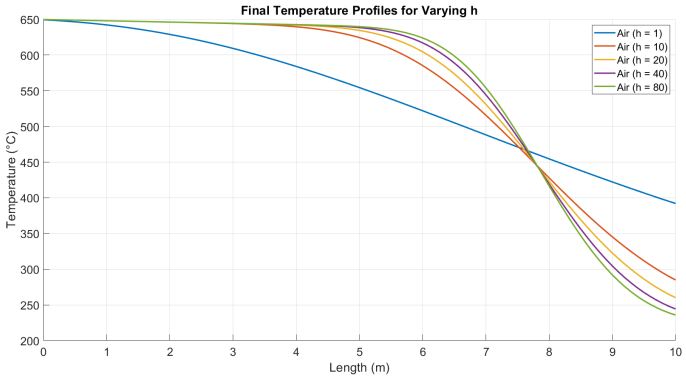

Figure A.4: Variation in convective heat transfer coefficient h during 24 hour operation ranging from 1-80 $(W/(m^2 \cdot K))$

Figure A.4 shows the temperature profile across the length of the bed for different values of the convective heat transfer coefficient h, ranging from 1-80 $W/(m^2 \cdot K)$. For all the cases, the temperature decreases along the bed length for the discharging cycle. As h increases, the rate of heat transfer increases, leading to a steeper temperature gradient along the bed. For higher h values, the fluid temperature drops more rapidly within the first few meters of the bed, indicating more effective thermal interaction. Conversely, for lower h values, the temperature decreases more gradually along the entire bed, showing weaker heat transfer and a more uniform temperature profile.